Magma flow, exsolution processes and rock metasomatism in the Great Messejana–Plasencia dyke (Iberian Peninsula)

Pedro F. Silva,[1,2] Bernard Henry,[3] Fernando O. Marques,[4] Eric Font,[2] António Mateus,[5] Ramón Vegas,[6] Jorge Miguel Miranda,[2] Ricardo Palomino[6] and Alicia Palencia-Ortas[7]

[1]*ISEL/DEC, R. Conselheiro Emídio Navarro, 1,* 1950-062 *Lisboa, Portugal. Email: pmfsilva@fc.ul.pt*
[2]*IDL/CGUL, Univ. de Lisboa, Lisboa, Portugal*
[3]*Paleomagnetism, IPGP and CNRS,* 4 *av. de Neptune,* 94107 *Saint-Maur cedex, France*
[4]*Dept. de Geologia and IDL, Faculdade de Ciências, Universidade de Lisboa, Lisboa, Portugal*
[5]*Dept. de Geologia and CEGUL, Faculdade de Ciências, Universidade de Lisboa, Lisboa, Portugal*
[6]*Dept. de Geodinámica, Facultad de C. Geológicas, Universidad Complutense de Madrid, Spain*
[7]*Dept. de Física de la Tierra, Astronomia y Astrofísica, Universidad Complutense de Madrid, Spain*

SUMMARY

Magma flow in dykes is still not well understood; some reported magnetic fabrics are contradictory and the potential effects of exsolution and metasomatism processes on the magnetic properties are issues open to debate. Therefore, a long dyke made of segments with different thickness, which record distinct degrees of metasomatism, the Messejana–Plasencia dyke (MPD), was studied. Oriented dolerite samples were collected along several cross-sections and characterized by means of microscopy and magnetic analyses. The results obtained show that the effects of metasomatism on rock mineralogy are important, and that the metasomatic processes can greatly influence anisotropy degree and mean susceptibility only when rocks are strongly affected by metasomatism. Petrography, scanning electron microscopy (SEM) and bulk magnetic analyses show a high-temperature oxidation-exsolution event, experienced by the very early Ti-spinels, during the early stages of magma cooling, which was mostly observed in central domains of the thick dyke segments. Exsolution reduced the grain size of the magnetic carrier (multidomain to single domain transformation), thus producing composite fabrics involving inverse fabrics. These are likely responsible for a significant number of the 'abnormal' fabrics, which make the interpretation of magma flow much more complex. By choosing to use only the 'normal' fabric for magma flow determination, we have reduced by 50 per cent the number of relevant sites. In these sites, the imbrication angle of the magnetic foliation relative to dyke wall strongly suggests flow with end-members indicating vertical-dominated flow (seven sites) and horizontal-dominated flow (three sites).

Key words: Magnetic fabrics and anisotropy; Rock and mineral magnetism; Large igneous provinces; Magma migration and fragmentation; Europe.

1 INTRODUCTION

Magma flow through fractures is believed to be an efficient mechanism for silicate melts to drift in the lithosphere (e.g. Platten & Watterson 1987; Lister & Kerr 1991; Ernst *et al*. 1995; Rubin 1995). However, in most cases, flow cannot be assessed by conventional geological methods. Anisotropy of magnetic susceptibility (AMS) reflects the orientation of minerals, therefore its use as a potential magma flow indicator (Khan 1962; Knight & Walker 1988; Hargraves *et al.* 1991). However, in many cases, the original magmatic rock is altered to different degrees by early high-temperature mineral exsolution and rock metasomatism and/or by late meteoric alteration; therefore, the effects of these phenomena on AMS were evaluated in the present study. Moreover, there is still great debate as to the relationship between the petrofabrics deduced from AMS and the magmatic flow within dykes. Therefore, we also investigated possible factors controlling this relationship. Despite these complexities, AMS has been widely used to infer petrofabrics related to magma flow (Cañón-Tapia 2004, and references therein for review of AMS applications to dykes), helping the characterization of complex intrusion conditions within lithosphere in different geodynamic settings (e.g. Henry 1974; Ernst & Baragar 1992; Callot *et al.* 2001; Archanjo *et al.* 2002; Geoffroy *et al.* 2002; Hrouda *et al.* 2002; Féménias *et al.* 2004; Silva *et al.* 2004; Borradaile & Gauthier 2006; Lefort *et al.* 2006).

Our objective was to study magma flow in deep-emplaced dykes with variable thickness. The dyke thickness at PO2, PO4, PO5 and VF is less than 6 m; in the remaining stations, it is thicker, reaching

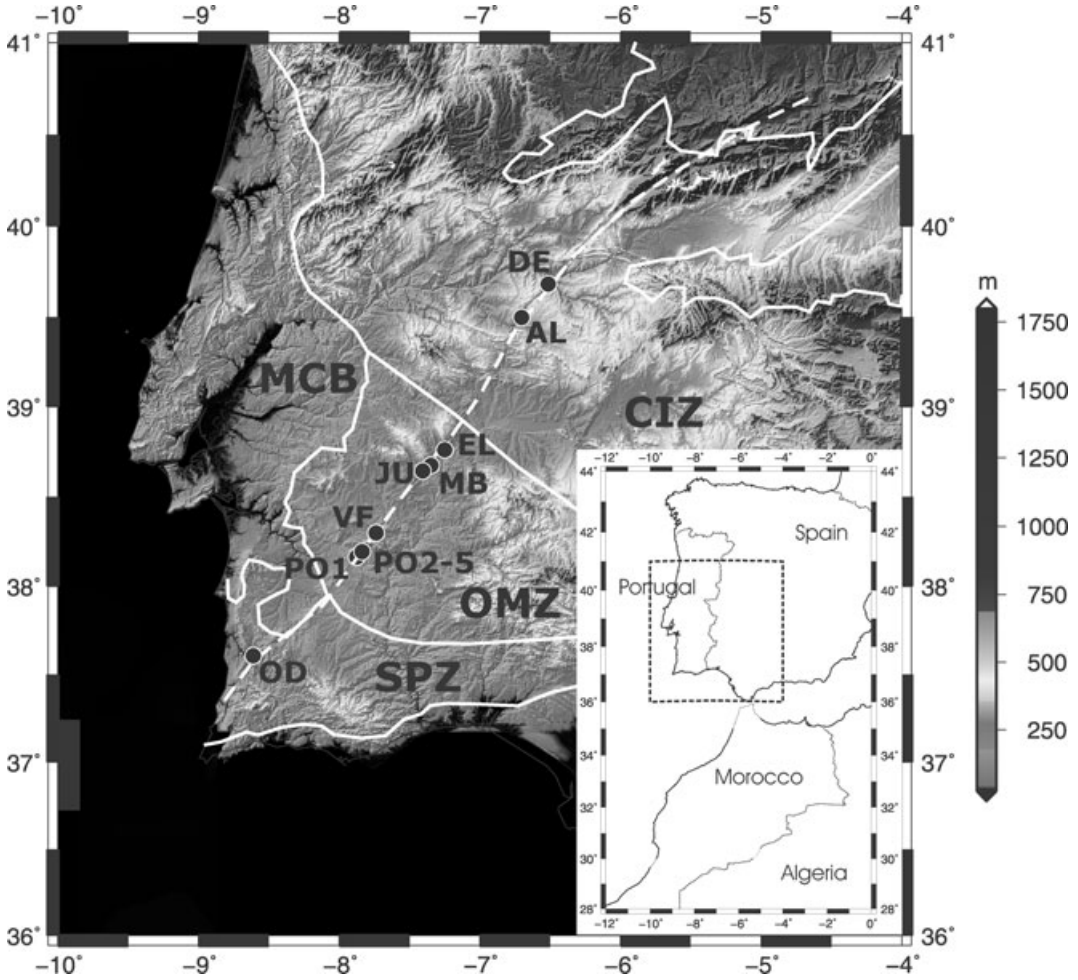

Figure 1. Studied area with location of sampling stations. White dashed line indicates morphological evidence of Messejana–Plasencia dyke presence. CIZ, Central Iberian Zone; OMZ, Ossa-Morena Zone; SPZ, South Portuguese Zone; MCB, Meso-Cenozoic Basin.

140 m at DE. Exsolution and metasomatic processes modify, to different degrees, the original mineral assemblage. Therefore, we evaluated the potential effects of exsolution and metasomatism on the magnetic properties of the studied rocks, by bringing together AMS work with detailed petrographic and scanning electron microscopy (SEM) analysis in selected samples. The Messejana–Plasencia dolerite dyke (MPD) in the Iberian Peninsula was chosen as a case study, and 360 samples were collected at 12 stations (Fig. 1 and Table 1). Whenever possible, sampling was performed along cross-sections perpendicular to the dyke walls to evaluate the variation of bulk magnetic properties and of the magnetic fabric. Following Tauxe *et al.*'s (1998) 'strategy' proposal, our sampling was more concentrated near the margins of the dyke.

The strong weathering, usually affecting dolerite, is a major problem in the MPD study. However, Krasa & Herrero-Bervera (2005) concluded that weathering promotes changes in bulk susceptibility and degree of anisotropy, but not in directions of the AMS ellipsoid principal axes. Anyway, the search for, and study of, well-preserved rocks along cross-sections was a primary goal. Only three stations (AL, DE and VF, Fig. 1) from a total of 12 allowed collection of samples along full cross-sections, running between the dyke walls to the core. At the remaining stations, sampling was strongly constrained by weathering effects and only partial cross-sections were sampled that, nevertheless, include measuring of distances to the dyke walls.

2 GEOLOGICAL SETTING

The MPD is a long igneous structure that belongs to the Central Atlantic Magmatic Province (CAMP), one of the large igneous provinces (LIPs) on Earth, related to the initial breakup of Pangaea (e.g. May 1971; Marzoli *et al.* 1999). The dyke, studied for many years in terms of its petrologic and geochemical features (e.g. Torre de Assunção 1949; Zbyszewski & Freire de Andrade 1957; Del Valle Lersundi 1959; Schermerhorn *et al.* 1978; Martins 1991; Vegas 2000; Cébriá *et al.* 2003), trends SW–NE for *ca*. 530 km, criss-crossing obliquely the South Portuguese, Ossa Morena and Central Iberian Zones of the Iberian Massif (Fig. 1). The actual length of the dyke can be even greater, since Cenozoic sediments of the Douro Basin cover part of its northern tip. Although the regional trend of the dyke is well constrained along the NE–SW direction, locally it reveals a segmented nature, often showing subparallel branches with variable thickness (ranging from 1 to *ca.* 140 m). The igneous body intruded a pre-existing fracture zone that was generated in Late-Variscan times (e.g. Marques *et al.* 2002). Recent $^{40}Ar/^{39}Ar$ radiometric ages of 203 ± 2 (Dunn *et al.* 1998) and 202.8 ± 2.0 Myr (Rapaille *et al.* 2003) suggests a narrow period of magmatic intrusion, in agreement with available palaeomagnetic data (Schott *et al.* 1981; Palencia-Ortas *et al.* 2006).

The outcropping rocks show only minor mineralogical variations from the margins (micro dolerite) to the core (dolerite, locally

Table 1. Main properties of studied sites.

Station	Latitude	Longitude	Thickness	Dyke	N	$K \pm$ SD	K_1	K_3	P'	T	Fabric
(site)			d/margin (m)	(S/D)		(10^{-3}SI)	(S/D)	(S/D)			
AL	39°34.3′	6°37.6′	∼100	215/80							
AL-SE1[a]			0.04 – 0.3/SE		14	9.8 ± 5.2	234/45	120/23	1.018	0.67	3
AL-SE2[a]			0.5 – 13/SE		14	18.6 ± 1.4	246/61	142/8	1.012	0.58	3
DE	39°45.7′	6°26.4′	∼140	240/80							
DE-NW1			0.8 – 2/NW		11	16.2 ± 4.5	182/28	62/43	1.016	0.11	3
DE-NW2			2 – 20/NW		17	22.9 ± 1.3	80/41	311/36	1.012	-0.14	2
DE-C1[a]			20 – 50/NW		19	25.6 ± 3.9	224/60	333/11	1.021	0.38	3
DE-C2			50 – 60/NW		9	21.6 ± 1.1	214/11	114/45	1.012	-0.71	1
DE-C3			60 – 80/NW		16	14.0 ± 7.7	79/11	343/28	1.014	0.23	2
DE-FL			80 – 82/NW		8	0.40 ± 0.02	106/1	15/35	1.001	0.44	3
DE-SE[a]			84 – 125/NW		15	21.8 ± 6.5	110/70	321/18	1.017	0.00	2
EL1	38°49.4′	7°11.6′	∼120	032/90							
EL1-NW			1 – 3/NW		11	25.5 ± 0.6	38/10	142/54	1.023	0.06	1
EL1-C[a]			50 – 60/SE		26	39.7 ± 24.9	191/64	309/13	1.015	-0.19	2
JU1	38°43.8′	7°17.1′	>30	065/90							
JU1-A			10 – 15/SE		5	24.8 ± 2.2	312/15	69/57	1.033	-0.33	1
JU1-B[a]			10 – 15/SE		8	24.5 ± 4.2	234/3	327/43	1.024	0.41	3
MB1	38°42.0′	7°21.0′	∼5	065/85							
MB1-NW[a]			1 – 3/NW		10	19.8 ± 3.9	52/34	322/0	1.023	0.75	3
MB2	38°42.2′	7°20.9′	∼120	040/90							
MB2-NW1[a]			1 – 3/NW		15	18.6 ± 1.4	230/30	137/7	1.020	0.70	3
MB2-NW2			30 – 45/NW		12	15.8 ± 1.1	179/30	87/5	1.011	-0.17	1
OD1	37°38.2′	8°34.5′	>40	076/90							
OD1-SE			1.5 – 3.5/SE		22	23.7 ± 5.0	11/21	252/52	1.020	-0.70	1
OD1-C			3.5 – 20/SE		27	18.3 ± 8.0	27/1	296/25	1.018	-0.95	1
PO1	38°14.5′	7°47,6′	∼100	030/90							
PO1-NW			1 – 3/NW		19	20.1 ± 0.6	190/21	91/22	1.018	0.13	2
PO2	38°18.0′	7°42.0′	∼4	040/90							
PO2-SE[a]			1 – 2/SE		13	7.0 ± 0.6	70/32	308/40	1.008	0.65	3
PO4	38°19.7′	7°42.2′	∼4	040/90							
PO4-SE[a]			1 – 2/SE		18	26.2 ± 2.6	63/63	309/11	1.032	0.79	3
PO5	38°20.9′	7°41.1′	∼4	040/90							
PO5-NW[a]			1 – 3/NW		14	20.8 ± 6.7	48/52	138/0	1.025	0.62	3
VF	38°12.9′	7°49.7′	∼6	040/90							
VF-SE1[a]			0.07 – 0.4/SE		26	4.2 ± 3.9	359/58	130/22	1.008	0.20	3
VF-C			3.3 – 3.8/SE		14	18.1 ± 3.9	273/35	22/24	1.010	0.11	2

Notes: d/margin, distance of sample to the nearest margin; Dyke, Strike and dip of the dyke; N, number of samples; K, bulk magnetic susceptibility; K_1, declination and inclination of the maximum susceptibility principal axis; K_3, declination and inclination of the minimum susceptibility principal axis; P', corrected degree of anisotropy; T, shape parameter; Fabric, type of magnetic fabric.

[a] Sites used for the flow determination.

gabbro) of the thick dyke. Petrologic/geochemical studies suggest a relatively uniform magma source (continental tholeiitic basalt), locally modified by assimilation of upper-crustal rocks (e.g. Martins 1991; Cebriá *et al.* 2003). These authors inferred the assimilation of lower-crustal meta-igneous granulites and concluded that the tholeiitic magma involved in the MPD genesis resulted from partial melting of an enriched lithospheric mantle source. Locally, in the core of the thick dyke at station DE, it is possible to identify a planar, subvertical, *ca.* 4-m-wide structure (Fig. 2) in clean-cut contact with the enclosing dolerite. This structure, labelled below as DE–FL, records effects of strong fluid circulation during early metasomatism, as shown by the petrographic analysis.

3 SAMPLING AND METHODS

More than 360 samples were collected at 12 stations, distributed along *ca.* 400 km of the MPD (Fig. 1 and Table 1). In each station, sites were sampled along cross-sections perpendicular to the dyke walls to evaluate the variation of bulk magnetic properties and of the magnetic fabric.

AMS was measured with KLY-3 and KLY-2 instruments. The anisotropy of anhysteretic remanence was acquired with an LDA-3A demagnetizer coupled with AMU-1A anhysteretic magnetizer and measured with a JR6 magnetometer. Thermomagnetic analyses, low-field magnetic susceptibility as a function of temperature, $K(T)$, were performed under argon controlled atmosphere, using a CS3 furnace coupled to a KLY3 Kappabridge. Acquisition of isothermal remanent magnetization (IRM) was done up to a maximum field of 2.5 T using an impulse magnetizer IM-10—30, and samples were subsequently measured with a JR-6 magnetometer. Hysteresis loops were performed with a laboratory-made translation inductometer within an electromagnet.

Several samples underwent petrographic analyses by both transmitted and reflected light microscopy. Petrographic studies were complemented by SEM observations and energy dispersive spectra (EDS) analysis, performed on carbon-coated rock fragments with a Jeol JSM-6360LV microscope and a Noran Instrument EDS analyser at Laboratoire des Mécanismes et Transferts en Géologie (LMTG, Université Paul Sabatier, Toulouse, France).

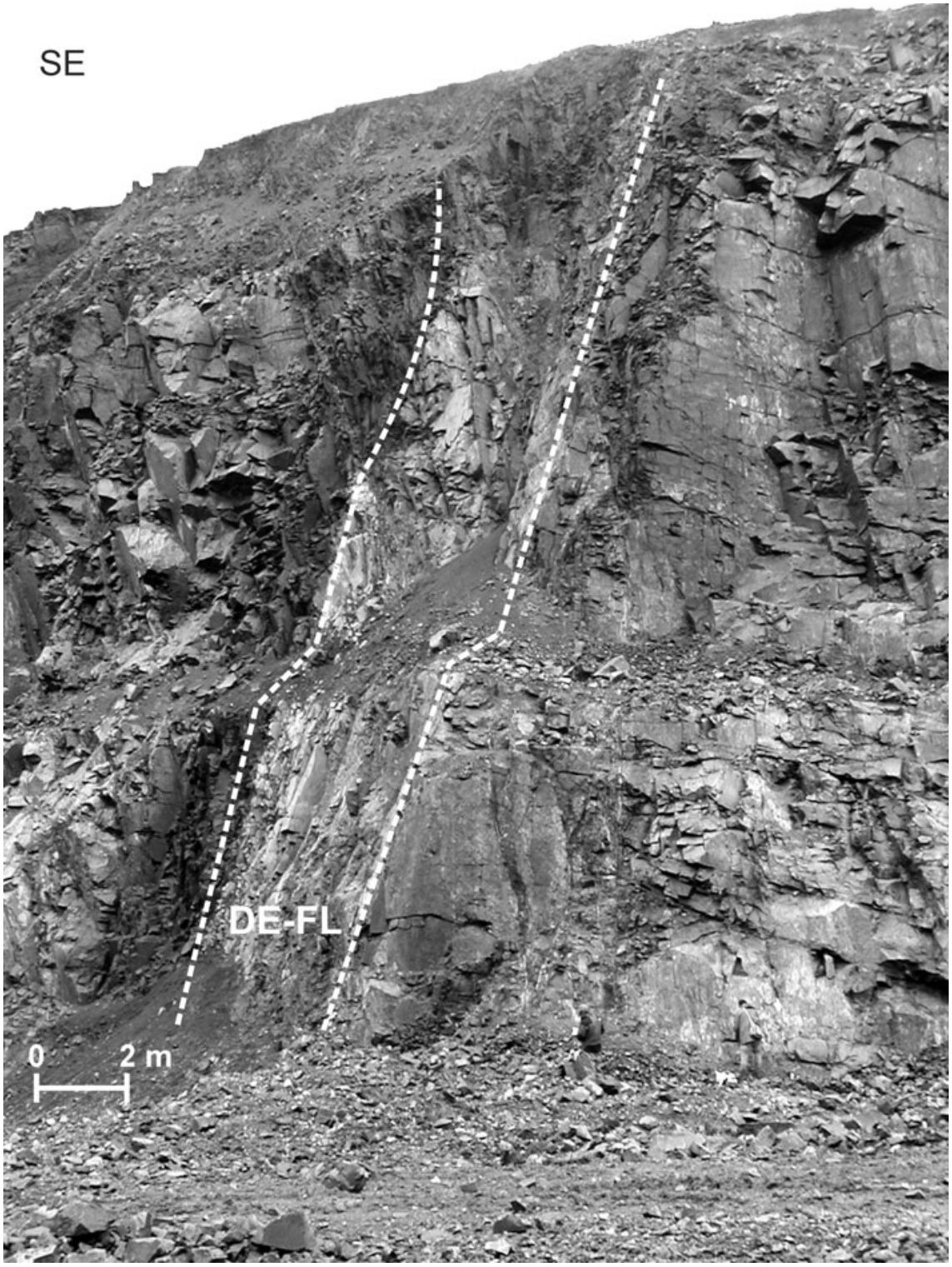

Figure 2. Picture of a segment of the dyke at station DE. Shaded lines delimit site DE-FL.

4 MICROSCOPY

Representative samples from AL, DE and VF stations (see Table 1) were selected for petrography under transmitted and reflected light microscopy. With the intention of checking the nature and origin of magnetic minerals in a finer scale, SEM/EDS analyses were also conducted at AL, DE, VF and OD1 stations. The selected samples were chosen to characterize the mineralogical features that are responsible for variations in thermomagnetic, bulk magnetic behaviour or distinct magnetic fabrics along cross-sections. The examined samples from these stations correspond to fine to medium grained dolerites.

4.1 Optical microscopy

4.1.1 Stations AL and VF

The selected samples were collected at distances d of 0.1, 0.15 and 36.5 m from the SE contact margin at AL (dyke thickness of *ca.* 100 m) and at 0.13, 1.7 and 3.6 m from the SE margin at VF (dyke thickness of *ca.* 6 m). These samples show mineralogical and textural features typically developed as a result of mild metasomatic processes, coeval with magma cooling (implying low contents of fluid components). Samples nearest the chilled margins ($d = 0.13$ m at VF-SE1 and $d = 0.10$ and 0.15 m at AL-SE1) have small amounts of opaque minerals. Primary magnetite usually occurs as irregular submicroscopic grains, forming microscopic clusters, randomly distributed within the silicate matrix. Accessory amounts of submicroscopic secondary magnetite grains occur along cleavage planes of some primary silicates (particularly clinopyroxene). Locally, optical effects due to late oxidation of magnetite (mainly controlled by inter- and transgranular fractures) are recognized; such oxidation leads to the development of more or less evident maghemite/haematite edges. Rare pyrite grains are also observed. Farther from the margin ($d = 1.7$ and 3.6 m at VF-C), samples display a slightly higher amount of opaque minerals, which can be grouped into two main types: (1) grains of magnetite with ilmenite exsolutions and (2) rare, irregular and submicroscopic grains of magnetite, occasionally in textural equilibrium with pyrite micrograins. For these two samples, there are no optical evidences of oxidation. In station AL, where the dyke is thicker, the sample closer to the core ($d = 36.5$ m at AL-SE2) displays distinct features when compared with previous specimens. Mixed microscopic grains of magnetite–ilmenite are relatively abundant, contrasting with rare interstitial magnetite (thinner and irregularly distributed, generally encircled by coarse silicates). Magnetite in mixed grains records effects of moderate to intense oxidation, being partly replaced by maghemite and haematite aggregates. Since primary silicates do not show evidence of weathering, magnetite transformations are ascribed to endogenous, relatively high-temperature oxidation processes, probably controlled by the local thickness of the intrusion.

4.1.1 Station DE

At this station (dyke thickness of *ca.* 140 m), samples were collected at 1.1, 21, 41, 52, 80, 81 and 85 m from the NW margin. All these specimens record effects of metasomatic processes synchronous with dyke cooling, which caused appreciable mineralogical and textural transformations.

In the incipiently metasomatized sample ($d = 41$ m at DE-C1), plagioclase and clinopyroxene occur in similar proportions, with accessory amounts of amphibole, Fe-Ti-oxides, biotite, apatite and scarce olivine, pyrite and chalcopyrite. Locally, quartz–feldspar granophyric intergrowths can be identified, developing internal arrangements and fine dendritic progressions towards the borders, which strongly suggest a relatively rapid magma cooling. The oxides do not exceed 5 per cent modal and include either micrometric euhedral to sub-euhedral grains of magnetite or millimetric sub-euhedral grains of magnetite, comprising short discontinuous ilmenite lamellae or thick ilmenite laths along the {111} spinel planes. Evidence for very slight spinel oxidation can be observed in some larger grains, usually recorded by thin maghemitic fringes.

Two samples ($d = 21$ m at DE-C1 and $d = 52$ m at DE-C2) preserve metasomatic effects of moderate intensity (Figs 3a–d), which can be deduced from: (1) partial hydration of pyroxene grains and their replacement by secondary amphibole aggregates; (2) incipient hydrolysis of plagioclase grains, with local development of fine-grained white mica and quartz; (3) almost complete olivine breakdown and replacement by very fine-grained mixtures of hydrous-phyllosilicates and micrometric grains of secondary magnetite; (4) partial to total replacement of biotite by chlorite; (5) late calcite deposition, sealing both interstitial voiding and late inter- and transgranular fractures and (6) oxidation of primary spinel grains in presence of non-altered pyrite. Oxides represent between 4 and 8 per cent modal. The sample from DE-C2 shows coarser (up to 1 mm) sub-euhedral grains of magnetite, devoid of ilmenite oxi-exsolution but partly replaced by maghemite. These grains coexist with profuse, larger and variably oxidized spinel grains that display thick ilmenite laths, leading to the typical sandwich texture developed under gradual cooling.

In sample at $d = 1.1$ m (DE-NW1), the metasomatic effects are more intense, although not enough to completely obliterate the primary mineralogical and textural characteristics typical of a dolerite rock. Secondary mineral parageneses are dominated by hydrous-phyllosilicates that form fine-grained aggregates, replacing partially or completely the former pyroxene, amphibole, olivine, biotite and plagioclase grains. Locally, some of these aggregates include micrograins of secondary magnetite that are regularly disposed (mimetic of the pre-existent crystal morphology) and show optical evidence of subsequent, slight oxidation. Primary oxides are micrometric in size and do not represent more than 5 per cent modal. The oxidation of primary magnetite, forming either isolated grains or intergrowths, is always evident and may be quite intense in some grains. In the latter situations, maghemitic replacement takes place along intragranular fractures. The metasomatic effects observed at $d = 80$ m (DE-C3; Figs 3e and f) are similar to those found at $d = 1.1$ m, despite the coarser granularity showed by the specimen, conspicuous interstitial development of secondary Na-rich plagioclase masses and significant differences in the oxide mineralogy: (1) secondary magnetite is lacking, (2) fine-grained chlorite aggregates are devoid of oxide grains and (3) ilmenite is the dominant primary oxide, occurring as irregular, large grains that preserve tiny haematite exsolutions or as microscopic, isolated euhedral grains optically free of any kind of exsolution or of oxidation products. Conversely, the primary spinel grains show invariably multistage oxidation, showed by the development of irregular haematite fringes over maghemite.

Samples located the farthest from the NW dyke wall ($d = 81$ and 85 m, DE-FL) represent products of exceptional intense multistage metasomatism (Figs 3g and h). Original sub-ophitic to ophitic textures of dolerite are strongly obliterated. Consequently, the Na-plagioclase groundmass, together with epidote, quartz (fine-grained and interstitial), chlorite (besides other very fine-grained hydrous phyllosilicates), sphene, calcite and pyrite, forms the main mineral (secondary) assemblage. Primary oxide grains are scarce, (sub-) micrometric in size and display, always, evidence of intense chemical corrosion and oxidation. Haematite spinel-pseudomorphs can be observed as well as almost complete oxidation of pre-existing ilmenite-magnetite intergrowths, leading to fine-grained aggregates composed of haematite + secondary Ti-oxides (probably pseudobrookite s.s.).

4.2 SEM

Sample from DE-C2 site shows the lowest concentration of iron oxides with a characteristic bimodal distribution. Coarser iron oxides are rare and represented by isolated Ti-haematite (or ilmenite) and Ti-magnetite (400 μm in width; Figs 4b and d). The Ti-haematite illustrated in Fig. 4(b) presents an hexagonal structure with the

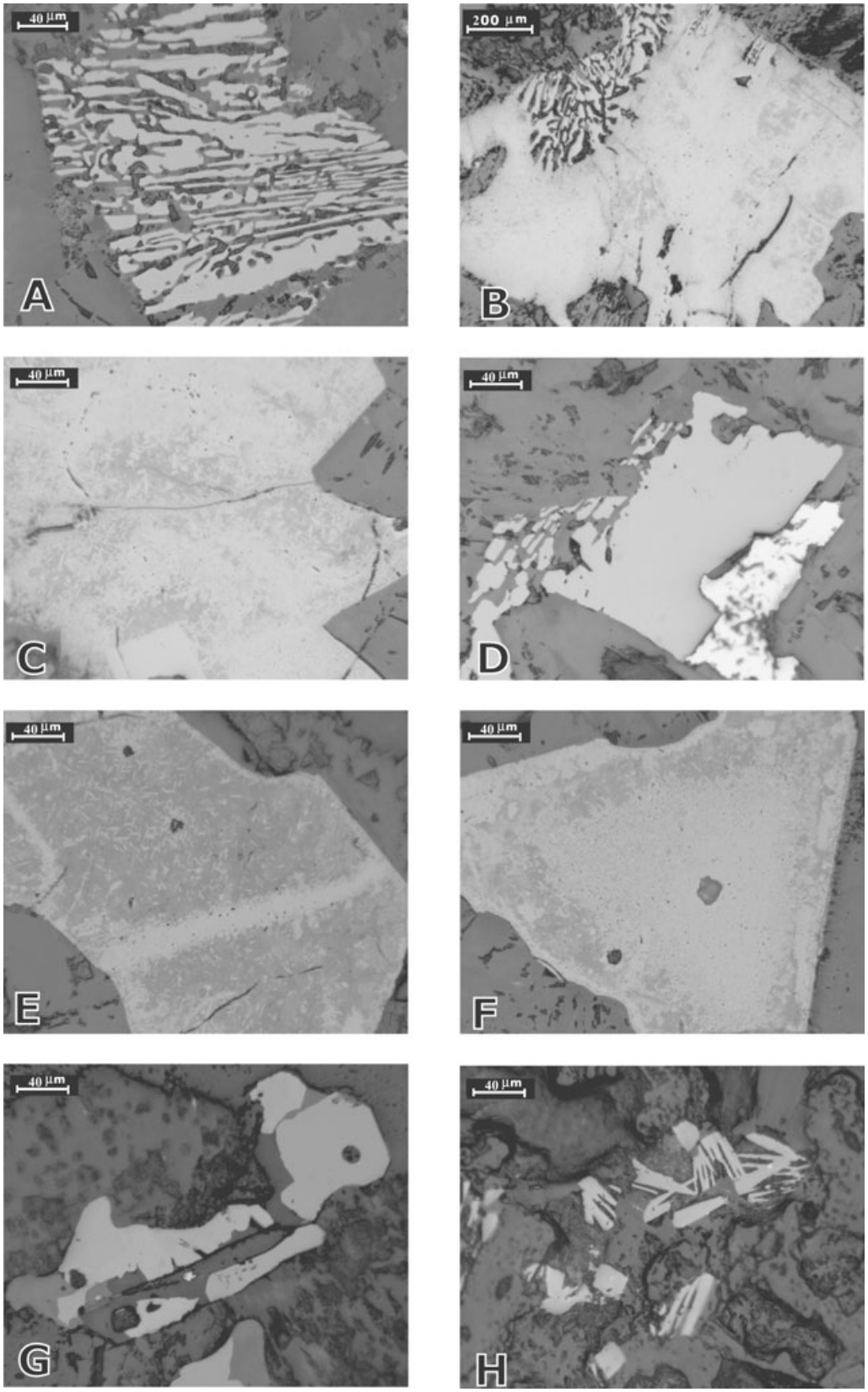

Figure 3. Examples of textural arrangements that result from different metasomatic/oxidation intensities. Sample from site DE-C1: (a) textural arrangement of incipiently oxidized magnetite developed as a result of rapid cooling; (b) strong oxidation of magnetite, producing maghemite ± haematite replacements, although preserving textures caused by rapid cooling; (c) maghemite ± haematite pseudomorphism of magnetite. Sample from site DE-C2: (d) coexistence of magnetite and pyrite (micrograins) without optical manifestations of oxidation. Sample from site DE-C3: (e) late intra-granular hematitic band; (f) haematite (± maghemite) pseudomorphism of magnetite. Samples from site DE-FL (g) magnetite micrograins coexisting with products of oxidation pseudomorphism (bluish-grain); (h) late haematite grains forming an interstitial cluster.

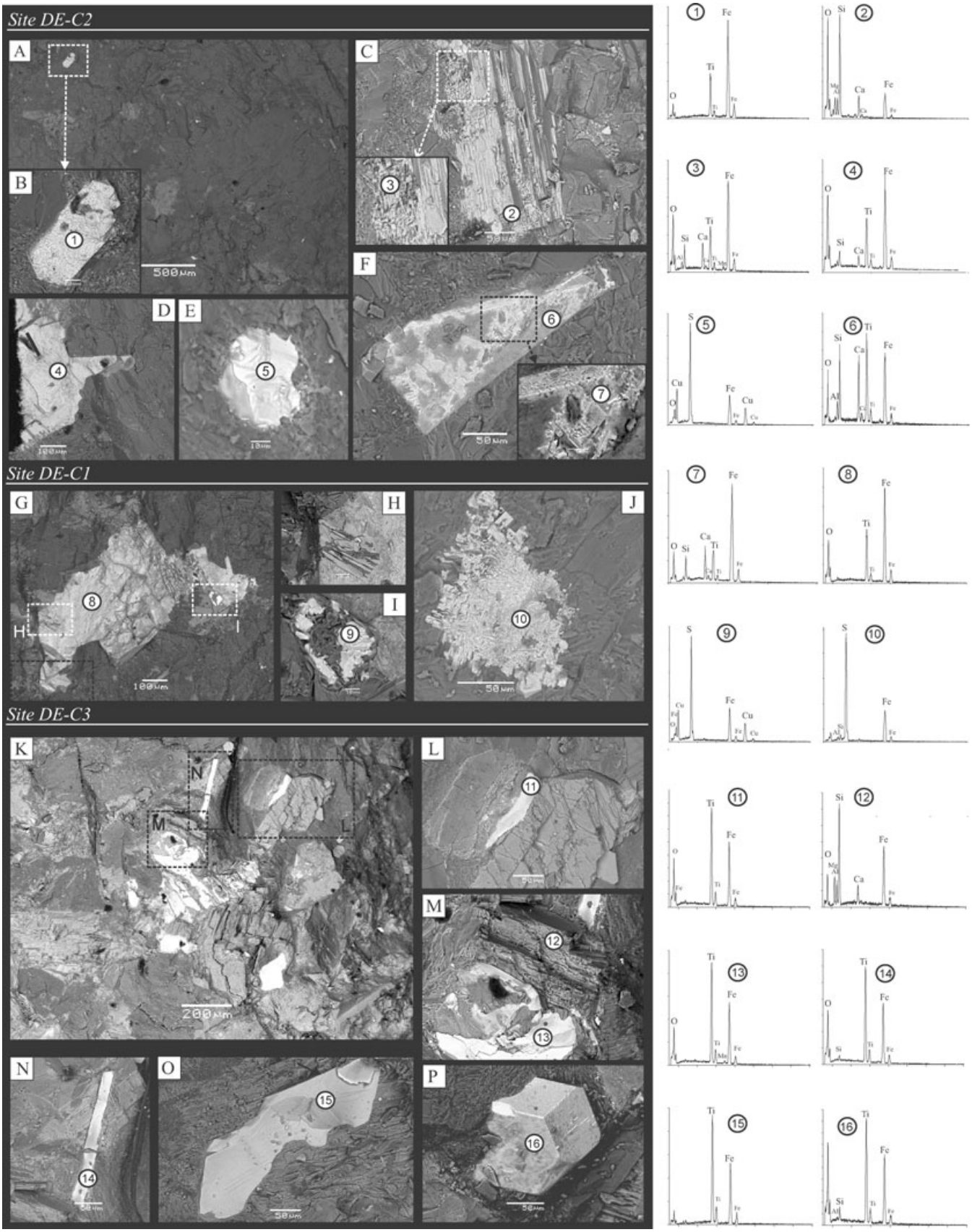

Figure 4. Scanning electron microscopy (SEM) and energy dispersive spectra (EDS) analysis of MPD samples (see text for details).

longer crystalline axis (∼160 μm) oriented perpendicular to those of adjacent silicate minerals (Fig. 4a). Most Fe and Ti-bearing oxides are localized along the cleavage planes of phyllosilicates (Figs 4c and f). Significant Ti and Fe peaks in EDS spectrum and typical exsolution textures suggest that these phyllosilicates are alteration products of the primary mineral assemblage that include Ti-magnetite, as it was already described by Perrin *et al.* (1991).

In comparison, samples from sites DE-C1 and DE-C3 show higher amounts of magnetic minerals dominated by a coarser population of euhedral and xenomorphic crystals of Ti-magnetite (400 × 700 μm) (Figs 4g–p). In samples DE-C1, Ti-magnetites are weakly altered to maghemite, as suggested by the darker fringes localized at the borders of the crystal (Figs 4g and h), but not exhibiting exsolution structures. DE-C3 is characterized by a mixture of coarse euhedral (mostly hexagonal) Ti-oxides (magnetite and haematite; Figs 4n–p) and relicts of primary Ti-magnetite, included in late phyllosilicates aggregates (Figs 4k–m). Locally, plate-like iron oxides (Ti-haematite or ilmenite) are observed included in a silicate phase (Fig. 4m). For both populations, the grain size of magnetic minerals is comprised between 100 and 250 μm. Xenomorphism and exsolution textures are absent or very weakly expressed, as noted in Fig. 4(p), where the exsolution lineation seems to have begun to form parallel to the long axis of the crystal. Sulphides are rare and represented by chalcopyrite and pyrite grains (Figs 4e, i and j); the former occur either as preserved (Fig. 4e) or corroded (Fig. 4i) grains; the latter occur as euhedral grains showing often striated structures.

Samples from sites AL-SE2, VF-SE and OD1-SE show similar magnetic carriers, mainly Ti-magnetite, but with different degrees of metasomatism and grain size. Site AL-SE2 displays an unimodal distribution of a Ti-Fe phase, represented by large (400–500 μm in width) sub-euhedral and xenomorphic grains, which exhibit numerous ilmenite exsolutions and are affected by maghemitization (Fig. 5a). Fig. 5(b) illustrates a silicate mineral neoformed into a pre-existent crystal of Ti-magnetite, showing ilmenite exsolution textures. Ti-free magnetite, probably of a secondary and late origin, is located and oriented along cleavage planes of silicate minerals (Fig. 5c). Compared with sample AL-SE2, specimens VF-SE and VF-C (Figs 5d–g) record a more intense mineral alteration due to metasomatism. In sample VF-SE, only fine (20–40 μm) Ti-magnetite (relicts), with ilmenite exsolutions, are found near to Fe–Mg–Ca silicate minerals (Fig. 5d). Similar features could be identified in sample VF-C. However, the coarser grain size of Ti-magnetite (60–140 μm) and the presence of Ti-Fe oxide relicts embedded in phyllosilicate aggregates suggest that in this sample, the metasomatic process did not totally obliterate the primary Ti-Fe oxides. In Fig. 5(f), the direction of the longer axis of the phyllosilicates is perpendicular to some structural lineations of primary Ti-magnetite. In sample VF-C late fluid circulation is locally suspected given the presence of Cu (-Sn) mineral phases (Fig. 5g).

In OD1-SE (Figs 5h–k), two populations of iron oxides are identified and correspond to (i) coarse (200 × 500 μm) and hexagonal Ti-Fe oxides, similar to those observed in sample DE-C3 but much more altered; and (ii) Ti-magnetite relicts (20 × 30 μm) with ilmenite exsolutions close to apatite (Fig. 5k).

5 ROCK MAGNETISM

5.1 Thermomagnetic curves

Thermomagnetic experiments were carried out on 50 samples. Under Ar-controlled atmosphere, the feature most common to all the experiments is a fast drop of $K(T)$ values at temperatures varying between 500 and 570 °C; these define Curie temperatures (see Petrovský & Kapička 2006) bracketed between 520 and 570 °C and close to the values obtained by Rochette *et al.* (1999) and Palencia-Ortas *et al.* (2006). This indicates the presence of Ti-poor magnetite as the main magnetic carrier (O' Reilly 1984; Dunlop & Özdemir 1997; Lattard *et al*. 2006). The presence of Ti-poor magnetite in samples from stations DE and MB2 is also suggested by the presence of the Hopkinson peak at around 550 °C (Fig. 6a). Mineralogical transformations during heating are minor in most samples as noted by the reversible behaviour of the curves (e.g. sample from station MB2, Fig. 6a); only some samples showed irreversible behaviour (e.g. samples from stations DE and EL1, Fig. 6a).

To better understand the origin of these mineral modifications, two complementary thermomagnetic experiments were performed for a sample, representative of irreversible cycles. These experiments were made in a non-controlled atmosphere, to increase the oxygen fugacity conditions (Fig. 6b). A first cycle (cycle 1) was made until a maximum temperature of 725 °C. A second experiment (cycle 2), with another powder of the same sample, was performed until a maximum temperature of 635 °C (point D) but momentarily interrupted during the heating run by cooling loops at points A (145 °C), B (255 °C) and C (420 °C). Most samples display similar heating curves, with a characteristic hump of $K(T)$ values for temperatures ranging between 250 and 350 °C. This hump is not visible on the cooling curve and should correspond to the transformation of maghemite into haematite during heating (Dunlop & Özdemir 1997), which is consistent with petrographic observations. This is confirmed heating steps from cycle 2. Curie temperatures around 560 °C confirm the presence of Ti-magnetite. Contrary to what was observed for the experiment performed under Ar-controlled atmosphere, susceptibility decreases up to temperatures above 640 °C, indicating the presence of haematite. Such haematite is probably not originally found in the samples but is the result of the transformation of maghemite. Stepwise heating experiments show that irreversible behaviour is reached at 420 °C, confirming that destruction of maghemite occurs between 255 and 420 °C. The observed higher $K(T)$ values during the cooling of cycle 1 are an indication that between 635 and 720 °C, some other transformation occurred with magnetite as a probable end product.

Both Ar- and non-controlled atmosphere experiments show that the primary magnetic mineralogy of most samples is preserved and essentially represented by Ti-magnetite. Simulation of oxidation processes by non-controlled atmosphere indicates haematite as a secondary product of maghemite alteration.

5.2 IRM analyses

IRM acquisition experiments were conducted on 37 samples from all stations. For most samples, saturation is reached for fields less than 300 mT (Fig. 7a), confirming Ti-poor magnetite as the main magnetic carrier (Lowrie 1990). For three samples, the presence of a high-coercive magnetic phase is also indicated by the non-saturation of the magnetization until 2.5 T. This component, interpreted as haematite, was only detected in samples that belong to the thinner segment (DE-FL) within DE cross-section. For this dyke segment, petrographic analysis revealed haematite as the result of an intense multistage metasomatism, mainly due to a local, preferential fluid circulation channel.

IRM curves were treated by the cumulative log-Gaussian (CLG) analysis (Robertson & France 1994), using the software of Kruiver

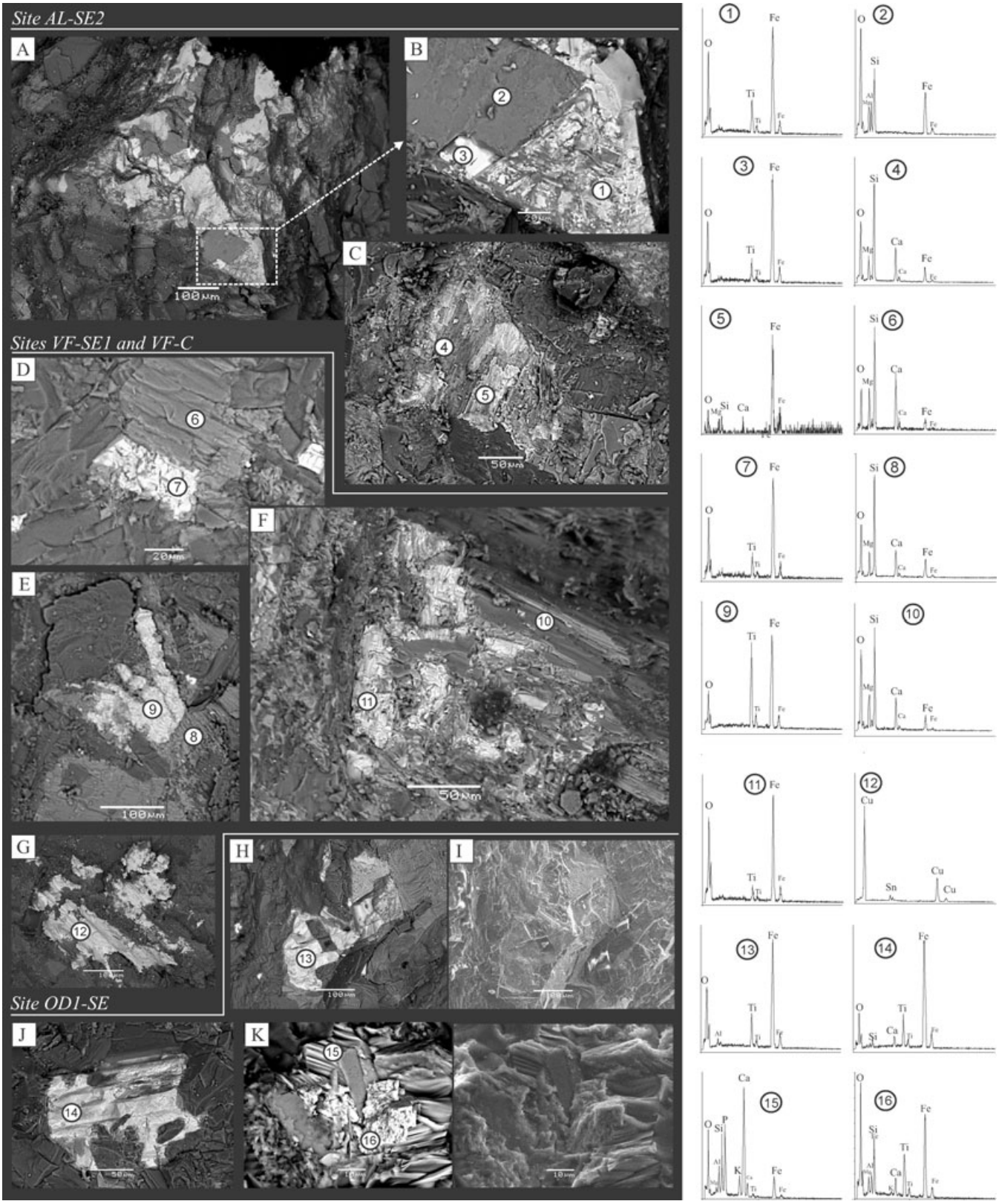

Figure 5. Scanning electron microscopy (SEM) and energy dispersive spectra (EDS) analysis of MPD samples (see text for details).

et al. (2001) (Fig. 7b). From these analyses, the presence of Ti-magnetite is inferred for all the analysed samples, contributing with 65 to 100 per cent of the saturation isothermal remanent magnetization (SIRM; component 1). Ti-magnetites present values of half-saturation field ($B_{1/2}$) ranging between 22.5 and 67.5 mT. For samples carrying haematite (component 3), the signal from this mineral contributes with 15 to 20 per cent of the SIRM signal, showing a strong coercivity ($B_{1/2}$ around 600 mT). For numerous samples

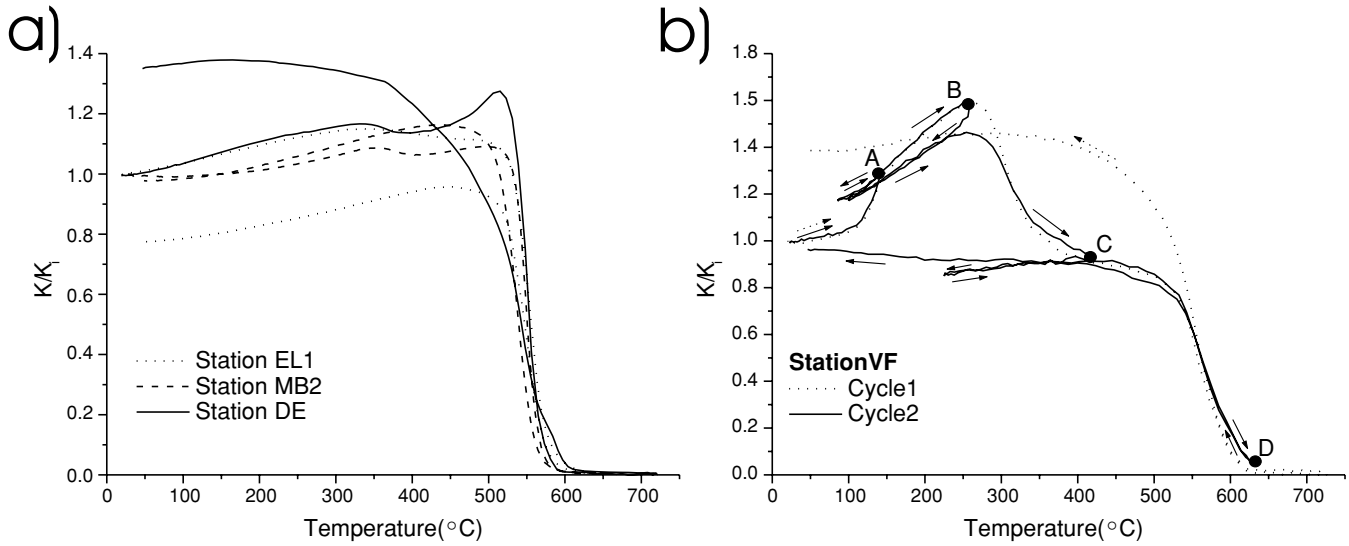

Figure 6. (a) Thermomagnetic behaviour of MPD samples performed under Argon controlled atmosphere. (b) Thermomagnetic behaviour of MPD samples, experiment performed under non-controlled atmosphere.

(observed in all the MPD segments sampled, excepting the thinner ones), the CLG model revealed a better fit when a third component was introduced (component 2). Such component contributes with 10 to 25 per cent of the SIRM and displays $B_{1/2}$ values bracketed between 16 and 40 mT, which partially overlaps with those of component 1 (e.g. of sample MB2–12 in Fig. 7b). Although these two intervals could correspond to Ti-poor magnetite with different grain size, the values of the dispersion parameter DP < 0.4 and of $B_{1/2} < 40$ mT are documented by Kruiver *et al.* (2001) for oxidized magnetite (i.e. maghemite, in the present case). Comparison of DP and SIRM values from components 1 and 2 allows clear distinction between maghemite ($0.30 <$ DP < 0.38 and SIRM < 150 A m^{-1}; Fig. 7c) and primary Ti-magnetite, for which SIRM values are broadly distributed between 0 and more than 800 A m^{-1}. Such variations in SIRM values could be related to different oxidation states (Wang *et al.* 2006) or to variations in Ti-content.

5.3 Hysteresis loops

Hysteresis loops with a maximum applied field of 500 mT were determined on 126 samples from all the stations (Figs 8a and b). The Day plot (Day *et al.* 1977) includes the limits and trending curves for single domain (SD)–multidomain (MD) mixtures determined by Dunlop (2002). It shows that most of the data follow the SD + MD mixing curves for the Ti-magnetite solid solution. However, for the saturation magnetization ratio (*Jrs*/*Js*) values above 0.2, a consistent shift to the right is observed, which suggests the presence of accessory minerals such as maghemite and haematite in addition to Ti-magnetite (Day *et al.* 1977; Dunlop 2002). No evidence of mixing with superparamagnetic grains (Dunlop 2002) appears. Note, additionally, that the intensity of bulk magnetic susceptibility *K*, mostly ranging from 10 to 25 in 10^{-3} SI, also agrees with the predominance of Ti-poor magnetite.

The group of samples located between 80 and 84 m from the NW margin of the dyke at DE station (DE-FL) are the only exception to the aforementioned features. For these specimens, the low *K* values ($0.3–0.6 \times 10^{-3}$ SI) suggest that paramagnetic and antiferromagnetic minerals play a significant role in the resulting magnetic fabric (Tarling & Hrouda 1993; Borradaile & Henry 1997). This interpretation is also supported by petrographic analysis, which points for an extreme multistage metasomatism, leading to intense chemical corrosion and oxidation of primary oxide grains in this particular domain of the dyke.

6 BULK MAGNETIC PROPERTIES ALONG CROSS-SECTIONS

To characterize variations in bulk magnetic properties, detailed analyses of *Js* and *K* were conducted along three MPD cross-sections. Distances were normalized by the half-thickness of the dyke. At station DE, *K* and J_s show the highest values at about half way between the medial plane and the margins. Towards the core and NW margin (no accessible outcrop at the SE margin), a gradual decrease of these parameters is observed, more pronounced for the domains nearest to the margins. Such pronounced decrease is also observed for domains nearest to the margins at stations AL and VF (Figs 9a–c).

The *Hcr/Hc* ratio for stations AL and DE are mostly limited between 1.5 and 2.1, with lower values observed for samples nearest the centre of the dyke (Fig. 9d). At station VF, part of the samples near the margin present values similar to those in other stations, but for the remaining samples this ratio goes much higher, reaching 2.7.

7 MAGNETIC FABRIC

To interpret AMS data, the parameters proposed by Jelinek (1981) were determined (corrected degree of anisotropy P' and shape parameter *T*), allowing the characterization of the AMS ellipsoid. Analyses of the principal magnetic susceptibility axes, defined as $K_1 \geq K_2 \geq K_3$, were made according to statistics for second-rank normalized tensors (Hext 1963; Jelinek 1978). The magnetic zone axis was determined by means of the bootstrap technique following the methodology in Henry (1997). The anisotropy of anhysteretic remanent magnetization (AARM) was computed from 18 components acquired along six different directions, using the AREF

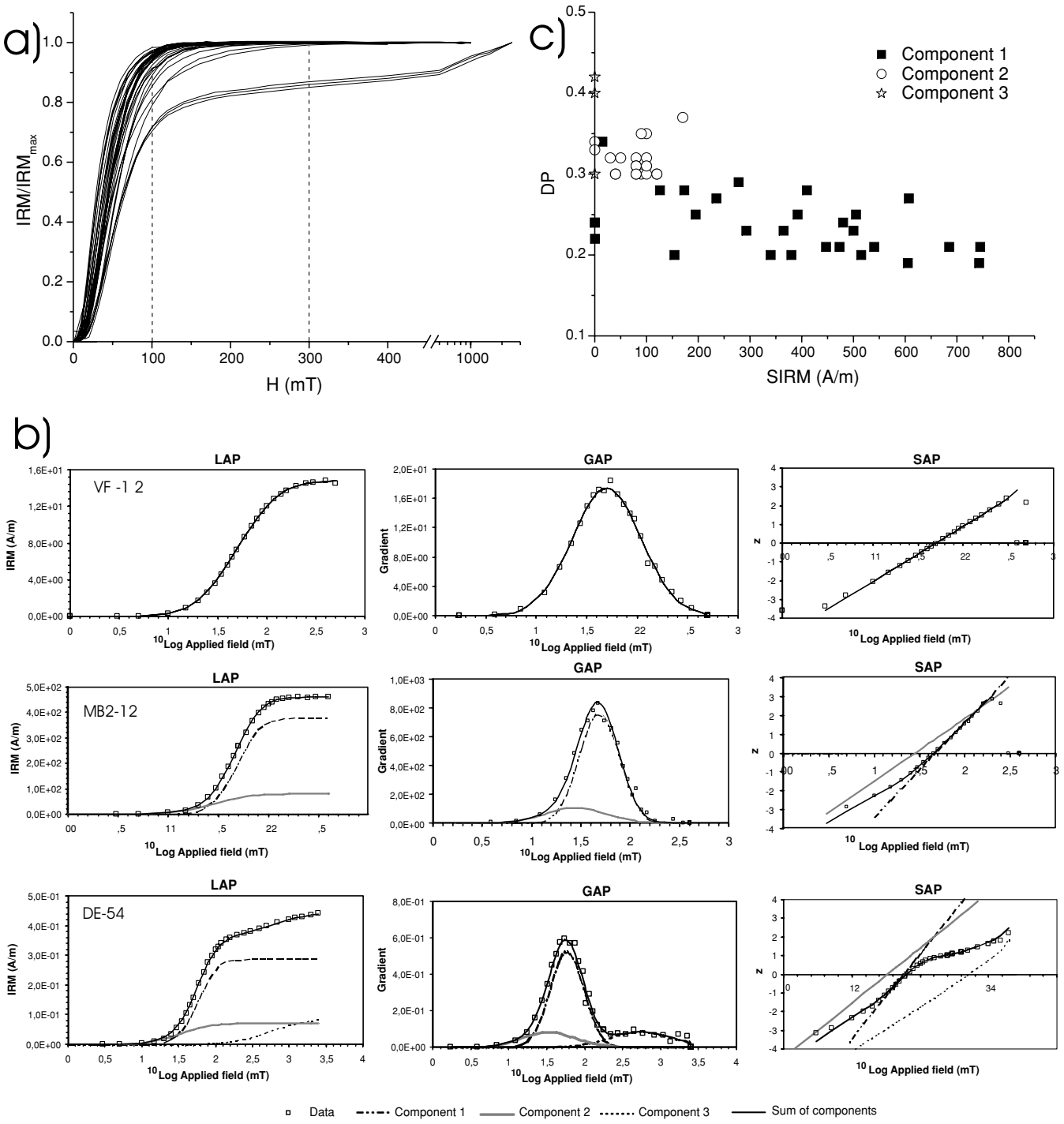

Figure 7. (a) Acquisition of Isothermal Remanent Magnetization; (b) Cumulative log-Gaussian analyses (Kruiver et al. 2001) for samples VF–12, MB2–12 and DE-54. LAP, Linear Acquisition Field; GAP, Gradient Acquisition Plot; SAP, Standardized Applied Field; (c) Saturation isothermal remanent magnetization (SIRM) versus dispersion parameter (DP).

software (AGICO). The principal AARM axes, here defined as $R_1 \geq R_2 \geq R_3$, were determined according to statistics for second-rank tensors (Jelínek 1996).

A detailed analysis regarding only the clustering defined by each principal axis (Fig. 10) enables the identification of different AMS fabrics, which comprise two end-members, magnetic fabrics type 1 and 3, with an intermediate fabric 2. Fabric 1 displays well-clustered K_1, whereas K_2 and K_3 are dispersed (Fig. 10a); the respective ellipsoid has a prolate shape (Fig. 11a) and the zone axis is well defined and aligned with K_1 (e.g. MB2-NW2 in Fig. 11b). Comparison of the AARM fabric with the AMS fabric (example of site OD1-SE, Fig. 10d) shows an exchange between R_3 and K_1 whereas R_2 and R_1 closely share the plane defined by K_2 and K_3. Fabric 3 shows well-grouped K_3, whereas K_1 and K_2 are often scattered (Fig. 10c); the respective ellipsoid has an oblate shape (Fig. 11a), and the zone axis shows an elongated confidence ellipse

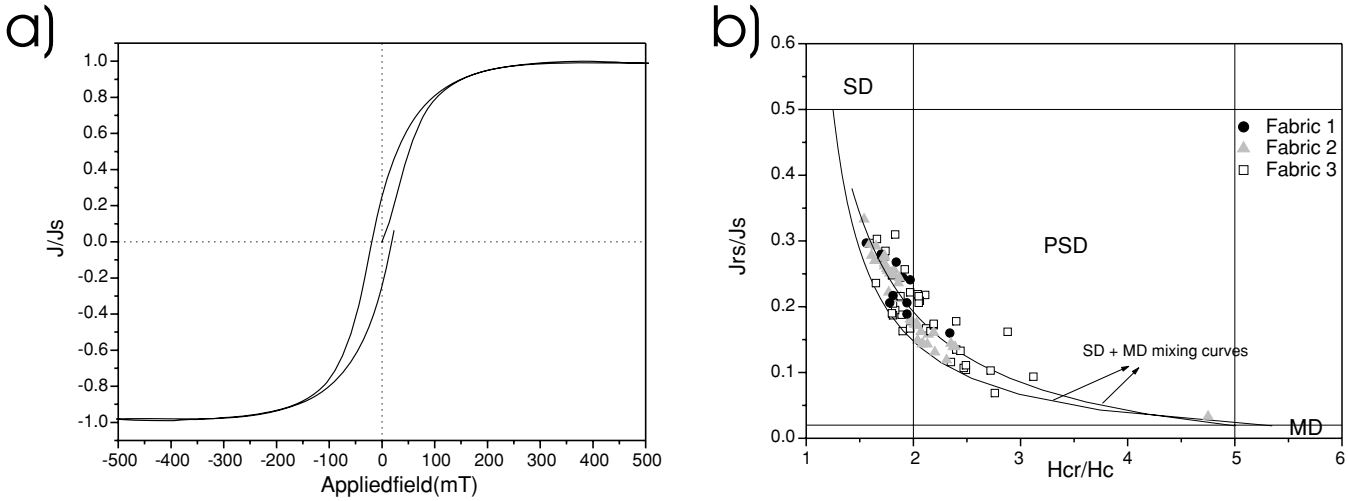

Figure 8. (a) example of hysteresis cycle, (b) Day *et al.* (1977) diagram with limits and mixing curves proposed by Dunlop (2002).

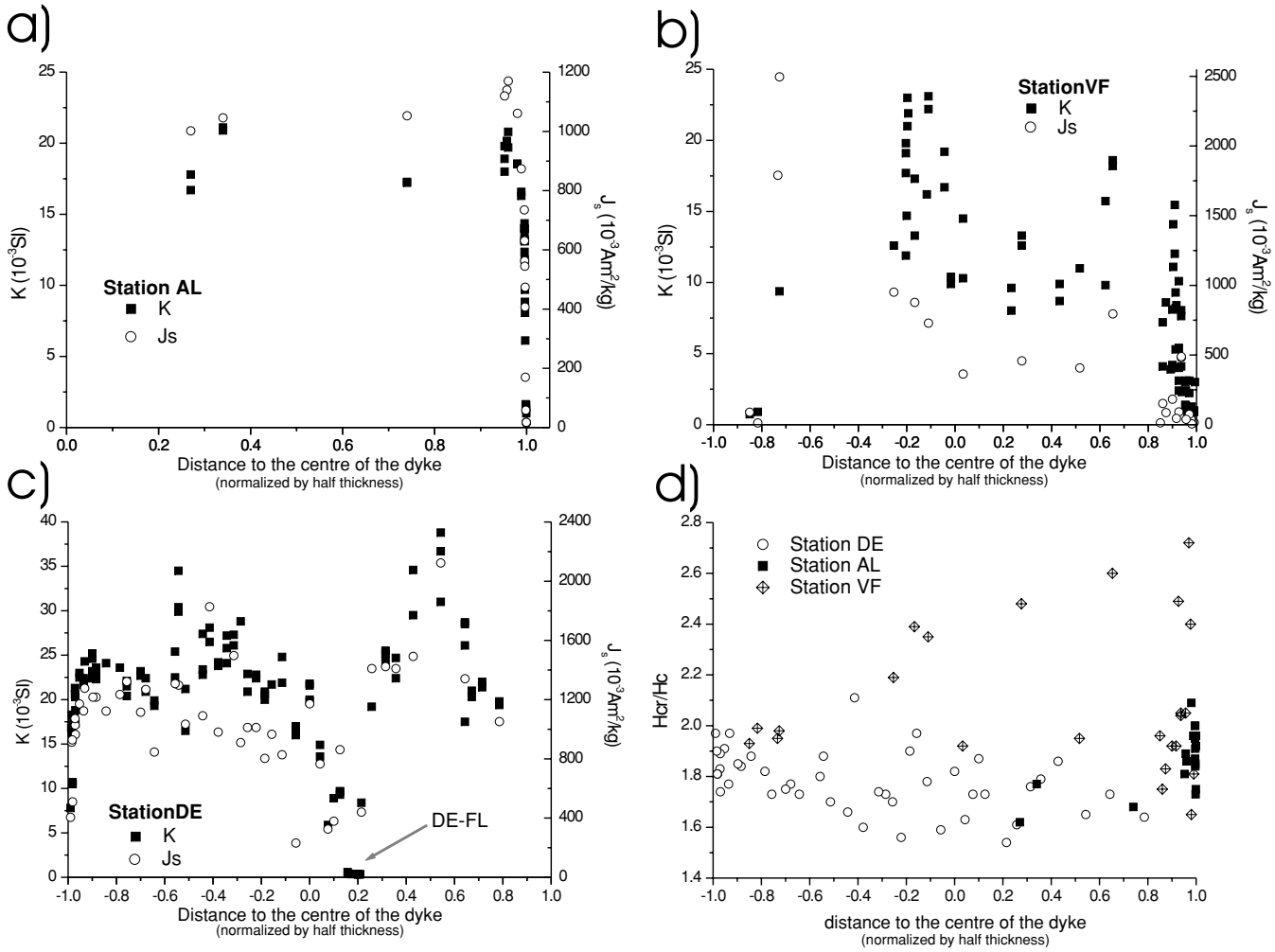

Figure 9. (a)–(c) Evolution of bulk magnetic susceptibility K and of the intensity of the Natural Remanent Magnetization (NRM) along cross-sections of the Messejana–Plasencia Dyke in stations AL (a), VF (b) and DE (c). (d) Evolution of the coercive ratio (Hcr/Hc) along cross-sections perpendicular to the MPD body. The distances are normalized by half thickness and measured relative to the centre of the dyke. Positive (negative) values of the distances increase towards SE (NW) margin.

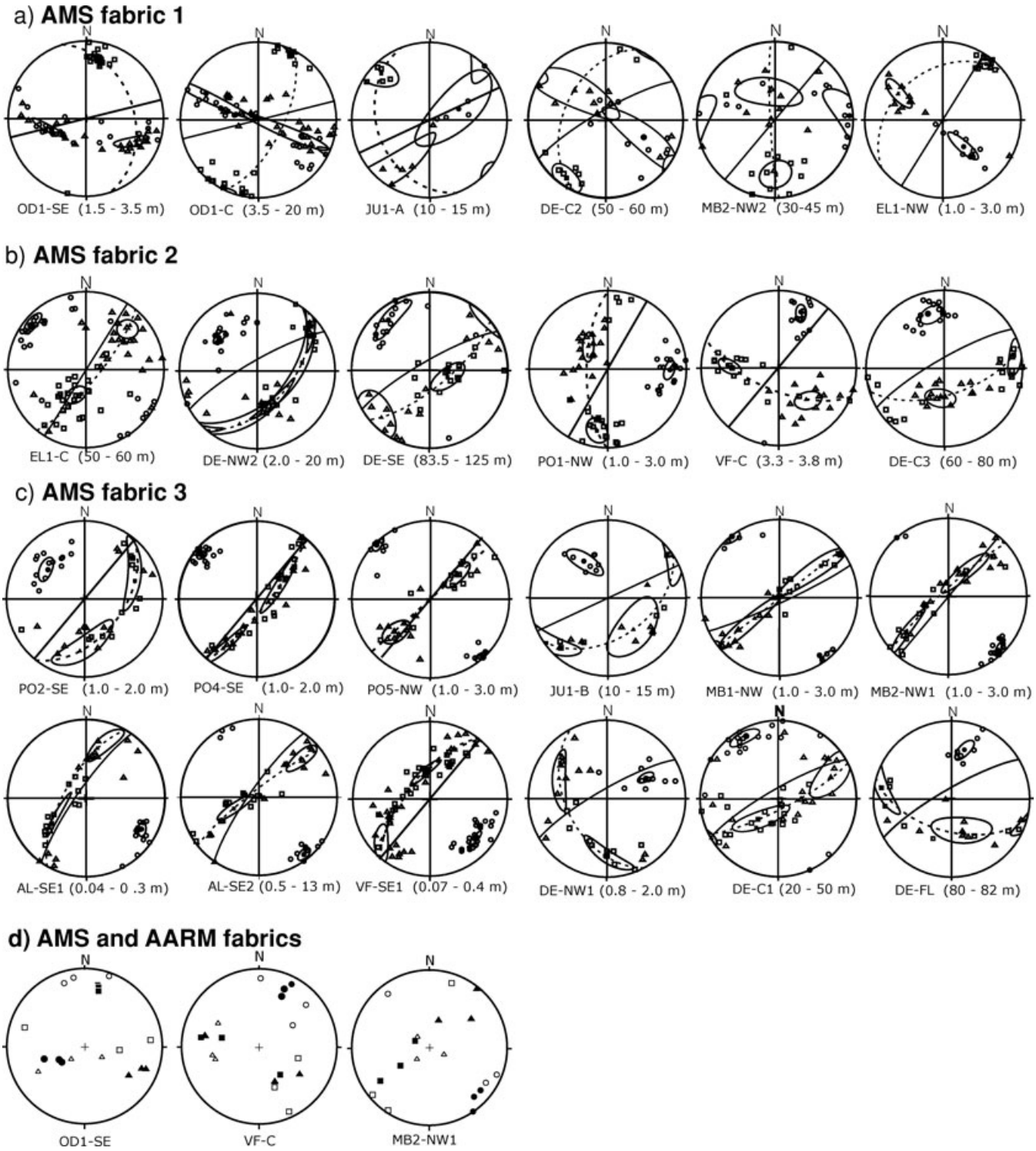

Figure 10. Lower hemisphere Schmidt stereographic projection for AMS: (a) Fabric 1; (b) Fabric 2 and (c) Fabric 3. Maximum K_1 (squares), intermediate K_2 (triangles) and minimum K_3 (circles) principal axes of the magnetic susceptibility ellipsoid. Solid line and dashed line corresponding to dyke and magnetic foliation planes, respectively. (d) AARM (open symbols) and AMS (black symbols) principal axes for fabric **1** (OD1-SE), fabric **2** (VF-C) and fabric **3** (MB2-NW1).

along the magnetic foliation plane (e.g. AL-SE1 in Fig. 11c). AARM principal axes likely define three clusters whereas AMS defines a magnetic foliation plane with K_1 and K_2 distributed along it (R_3 and K_3 share similar orientation; see example of MB2-NW1, Fig. 10d). Fabric 2 shows the three axes well defined (Fig. 10b); the ellipsoid corresponding to this fabric is mainly neutral (Fig. 11a) and the zone axis confidence ellipses are similar to the ones observed for fabric 3. The AARM ellipsoid mainly shows an exchange between K_1 and K_2 in comparison with AMS (example of VF-C, Fig. 10d), whereas K_3 axes remain invariant.

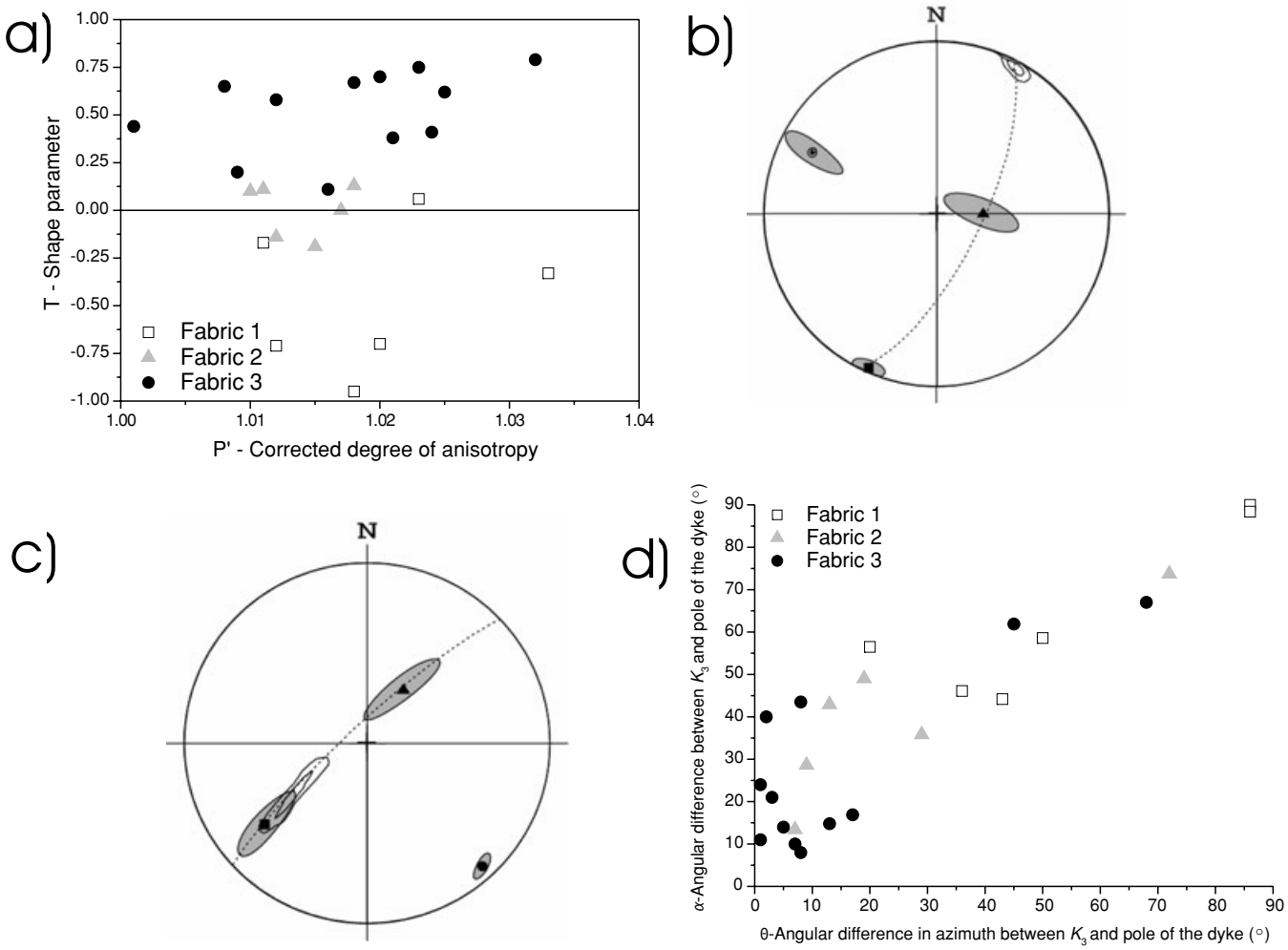

Figure 11. (a) Corrected degree of anisotropy P' versus the shape parameter T (Jelinek 1981), for the three distinct fabrics. Examples of zone axis confidence ellipses for sites MB2-NW1 (b, Fabric 3) and OD1-SE (c, Fabric 1) with confidence zones at 95 and 63 per cent of the 10 000 bootstrap re-sampling. Dashed line represents the magnetic foliation plane. Confidence zones of magnetic susceptibility principal axes correspond to grey areas, squares, triangles and circles corresponding to the maximum K_1, intermediate K_2 and minimum K_3 principal axes, respectively. Stereographic projection in the lower hemisphere. (d) Angular difference (in azimuth) between K_3 and dyke pole for different sites; angles in degrees.

Regarding the intensity of the susceptibility ellipsoid, one may conclude that P' values are low, mainly scattered between 1.010 and 1.035. Furthermore, the P' values do not show any correlation with the magnetic fabric type.

Comparing magnetic foliation and dyke plane orientations (angle α between poles to planes, and angle θ between strike of foliation and dyke planes, Fig. 11d), differences appear according to fabric type. For fabric 3, all sites but four have $2^\circ < \alpha < 25^\circ$. All samples with $\alpha < 30^\circ$ and PO2-SE and JU1-B, display a small $0^\circ < \theta < 19^\circ$, which means that the angular variations between these planes concerns mostly their dip. Sites with type 1 fabric show $\alpha > 40^\circ$ and $20^\circ < \theta < 90^\circ$ (Fig. 11d). Fabric 2 shows mixed behaviour, with angular differences between 10° and 75° for both α and θ.

In cross-sections where different fabric types characterize neighbouring sites (sections VF, JU1 and DE), the simple comparison of axes orientation yields important information, likely showing in most cases close clustering but with exchange between axes. In VF, JU1 and DE sections (except DE-NW1), fabric 3 denotes a magnetic foliation whose direction is subparallel to the dyke plane. However, mean K_3 at VF-SE1 (fabric 3) is similarly oriented to K_2 of VF-C (fabric 2), and mean K_3 at JU1-B (fabric 3) is similarly oriented to K_1 at JU1-A (fabric 1). At DE, the same observation is valid for DE-NW1 (fabric 3) and DE-NW2 (fabric 2), with permutations K_1–K_3, K_2–K_1 and K_3–K_2.

8 DISCUSSION

8.1 Metasomatism and bulk magnetic properties

Microscopic observations and rock magnetic studies show that Ti-poor magnetite is the main magnetic carrier of the studied samples. In general, these rocks preserve effects of slight to moderate metasomatism that took place after an early stage of high-temperature oxidation-exsolution event experienced by pre-existing Ti-spinels, which lead to mixed ilmenite-magnetite grains (e.g. Perrin *et al.* 1991). This early stage was coeval with initial stages of magma emplacement/cooling, under temperatures ranging from 1000 to 680 °C, if chemical compositions of primary oxides are assumed to be similar to those reported by Martins (1991). The onset of the superposed replacement of magnetite by maghemite at and along the spinel-ilmenite interfaces denotes subsequent oxidation at

sub-solidus equilibrium under *ca.* 600 °C (deuteric oxidation), involving residual magmatic fluids (e.g. Waychunas 1991; Topplis & Carroll 1995).

For the specific case of dykes, a cooling rate gradient is expected along cross-sections, therefore promoting differences on the progression of exsolution and metasomatic processes. The dyke thickness is another important variable, because it tends to correlate inversely with the cooling rate. This increases the time span needed for mineral phases to (re-) equilibrate under a specific evolving trend of temperature and redox conditions, with implications for the magnetic minerals in terms of assemblage, concentration and domain state. Homogeneous and smaller magnetite grains prevail near the dyke margins, whereas composite larger oxide grains (magnetite with ilmenite lamellar exsolutions) occur in the dyke core. These differences can be explained on the basis of mineral behaviour as a function of the cooling rate and redox conditions, expected to vary considerably from the dyke margin to its core in the presence of a large magma influx that evolves in an open system. These mineralogical features explain differences of Curie temperatures found in MPD thicker segments at AL and DE, where core sites are mostly characterized by slightly higher values (550–570 °C) than those at the dyke margins (520–540 °C). At VF, where the dyke is only 6 m wide, values for specimens representative of core and margin sites are quite similar, indicating the non-existence of conditions to sustain a significant cooling gradient across this thin MPD segment.

Although coarser grains are observed at the core of the dyke, the exsolution of Fe-Ti oxide minerals, evident for the composite grains with Ti-rich (mainly lamellar ilmenite) and Ti-poor regions (magnetite), generated solid-state diffusion of Fe and Ti cations and contributed to an effective decrease of the magnetic phase (e.g. Wilson *et al*. 1968; Ade-Hall *et al*. 1971; O'Reilly 1984; Butler 1992). Wilson *et al*. (1968) verified for a thick lava flow that, due to the same oxidation process, the exsolution of ilmenite lamellae is able to produce small isolated grains of Ti-magnetite, where the overall grain size is large. SEM analyses from MPD confirmed that ilmenite–magnetite exsolution present in some domains of the dyke is able to reduce magnetite grains to sizes below 1 μm, which could explain the presence of low coercive ratio values for domains nearest the core of the dyke for the thickest segments (AL and DE; Fig. 9d).

In general, *K* intensity and *Js* values show the lower values in samples nearest the dyke margins. It is known that these two bulk magnetic parameters are sensitive to the concentration, composition and grain size of Ti-magnetites (e.g. O'Reilly 1984; Dunlop & Özdemir 1997). The observed range of values, both for the Curie temperature and hysteresis ratios, cannot explain alone the variations of *K* intensity and of *Js* obtained along the sampled cross-sections (Hunt *et al.* 1995). These variations can be justified by the modal percentage of ferromagnetic carriers, as confirmed by petrographic observations. In dolerite dykes, the relative abundance and dimension of oxide mineral phases strongly depend on the cooling rate, once it determines the crystallization rate during the magmatic differentiation process. *K* intensity and *Js* are thus two magnetic parameters indirectly sensitive to the cooling rate in the studied dyke.

Hydration, hydrolysis and oxidation are the main processes involved in the metasomatism of low to moderate intensity recorded by a large number of MPD samples. Exceptionally, a higher fluid/rock ratio can considerably amplify the intensity of the metasomatic processes experienced by the primary mineralogy. Oxide mineral phases record successive stages of oxidation, which are synchronous of the hydration and hydrolysis processes involved in the breakdown of primary Fe-Mg silicates (including, therefore, the development of secondary magnetite) and in the progression of alkali and earth-alkali chemical reactions. These mineral transformations occur, therefore, as a response to succeeding metasomatic stages that characterize dyke cooling under temperature conditions ranging from *ca.* 550 to 400 °C. During this evolution, adequate conditions for extreme oxidation may be attained locally as a result of higher fluid/rock ratios, potentially increased by heterogeneous fracturing, and of the contribution of external, oxidizing fluid sources. At DE-FL, the metasomatism record is outstanding, although local, as deduced from almost complete oxidation of pre-existing ilmenite–magnetite intergrowths, leading to fine-grained aggregates composed of haematite + secondary Ti-oxides (pseudobrookite s.s.?), which according to Ade-Hall *et al.* (1968, 1971) resembles the 'higher class of iron-titanium minerals oxidation'. The weakest *K* and *Js* intensities, as well as the clear evidence for haematite from IRM experiments, add to petrographic observations. Moreover, for core domains of the dyke, a gradual decrease of these bulk magnetic parameters exists towards the thinner segment DE-FL (Fig. 9c). This evolution is in close correlation with the increase of the metasomatic transformations mainly due to an increase of the fluid/rock ratio, as recorded by the mineral-textural new arrangements observed in petrography.

Based on the overall MPD petrogenetic characterization and considering the mineral chemistry data that allow to constrain the stability fields of the prevailing dyke-forming phases (Martins 1991), a bulk pressure varying from 0.05 to 0.1 GPa has been inferred by de Bruijne (2001), pointing to a dyke emplacement between 2 and 4 km depth and a relatively rapid cooling path. This depth estimate is in good agreement with an apatite fission track study in granitic rocks hosting the MPD, which suggests that the sampled dyke was emplaced at a depth of 2–3 km, assuming a palaeo-geothermal gradient of $28 \pm 5\,^{\circ}\mathrm{C\,km^{-1}}$.

8.2 AMS fabric and magma flow

8.2.1 Metasomatic Effects

According to microscopic observations from DE section, the metasomatic effects (hydration, hydrolysis and oxidation) are moderate, with a gradual increase towards the core of the dyke from sites DE-C1 to DE-C3. On the contrary, they are very strong for site DE-FL. Comparison of the magnetic fabric in the neighbouring sites, DE-C3 and DE-FL, shows that in these sites, the AMS axes have similar orientation and similar shape of the susceptibility ellipsoid (Table 1). That is not the case for the mean P' values, which are 1.001 (ranging between 1.001 and 1.002 for specimens) in DE-FL and 1.013 (ranging between 1.004 and 1.020 for specimens) in DE-C3. With the exception of DE-FL, mean P' values vary between 1.012 and 1.021, in DE sites. The different values of P' are positively correlated with *K* values. In site DE-FL, where metasomatic effects are strong, replacement of pre-existing ilmenite–magnetite intergrowths by other phases (including phyllosilicates) was almost complete. Therefore, the influence of metasomatism on magnetic fabric seems to be similar to that of weathering (Krasa & Herrero-Bervera 2005), that is, no significant effect except for the intensity of the fabric and bulk magnetic susceptibility.

8.2.2 Exsolution effects

The slower cooling rate toward core domains of the thick segments of the dyke, which took place at the early stages of

magma emplacement for temperatures ranging between 1000 and 680 °C, favoured the development of magnetite–ilmenite lamellae exsolutions within the primary Ti-magnetite grains, leading to an effective strong decrease of the size of the magnetic grains. This implies a corresponding increase in the amount of SD grains.

For the sites studied by SEM analyses, the latter indicate that magnetic carriers in MPD rocks experienced intense exsolution processes, except for sites DE-C1 and DE-C3, where large and euhedral Ti-iron oxides, free (DE-C1) of or with very weak expression (DE-C3) of exsolution, are the principal magnetic carriers. DE-C1 shows a type 3 fabric and DE-C3, a type 2. Sites DE-C2 and OD1-SE, where exsolution is pervasive, show only type 1 fabric. Where the exsolution processes were intense but only partially affecting the iron oxides population (sites AL-SE2, VF-SE1 and VF-C), samples show fabrics 2 and 3. Furthermore, Day plot suggests a variation of the relative proportion of SD and MD populations with the type of magnetic fabric (Fig. 8b). Values of coercive ratio (Hcr/Hc) mostly range between 1.5 and 2.0 for fabric 1, between 1.5 and 2.5 for fabric 2 and between 1.5 and 3.25 for fabric 3, indicating that in samples with fabric 1 the contribution of SD grains might be more important than in the other fabric types. Finally, the comparison between AMS and AARM fabrics shows an exchange between K_1 and K_3 for fabric 1 (inverse fabric), an exchange between K_1 and K_2 for fabric 2 (intermediate fabric) and an agreement between principal axes for fabric 3 (normal fabric). Therefore, these results suggest the presence of an intimate relationship between that exsolution processes experienced by primary titanomagnetite grains at high temperature. The relative proportion between magnetite particles with SD and MD grain sizes results in complex permutations between axes (Rochette *et al.* 1999; Ferré 2002). This could be due to the fact that exsolution structures are highly magnetic and could dominate, even in low concentration, the magnetic state of the samples. Their internal structure wields a strong influence by transforming from a multidomain grain into an assemblage of magnetostatically interacting single-domain prisms (Feinberg *et al.* 2006). Feinberg *et al.* (2006) suggested that magnetic states are controlled by the shape anisotropies of individual magnetite prisms, magnetostatic interactions between closely spaced prism stacks and the shape anisotropy of the needle itself. In the case of the MPD dolerite, one could estimate the width of each prism to ∼20 μm, with a thickness lower than 1 μm, thus suggesting a magnetic behaviour near the SD. Such thin grains are known to behave as SD particles susceptible to invert K_1 and K_3 axes (Stephenson *et al.* 1986; Potter & Stephenson 1988; Rochette 1988; Dunlop & Özdemir 1997).

8.2.3 Magma flow and dyke Emplacement

Before any interpretation of magma flow direction, the criterion to choose sites relevant for flow determination has to be established. There is still debate about how to determine flow from AMS, hence we present a concise summary of the main points and justify our choice.

By studying a large number of dykes in Hawaii, Knight & Walker (1988) observed a good agreement between K_1 attitude and independent mesoscopic flow related structures; therefore they proposed the use of K_1 as an indicator of magma flow direction. However, the meaning of K_1 as the preferential magma flow indicator is not always verified (e.g. Baer 1995; Moreira *et al*., 1999; Geoffroy *et al.* 2002; Callot & Guichet 2003). According to Geoffroy *et al.* (2002), K_1 can represent an intersection lineation due to the superposition of planar and flow-related subfabrics, therefore showing significant angular deviations from the true magma flow direction. According to Callot & Guichet (2003), in such cases K_1 should change from a magnetic lineation related with magma flow to a zone axis as defined by Henry (1997). Once the stability of the magnetic foliation is demonstrated, even under the superposition of subfabrics, Callot & Guichet (2003) proposed the use of imbrication between magnetic foliation and dyke plane as a reliable tool to determine flow sense according to the method developed by Geoffroy *et al*. (2002).

Magma flow under a strain regime dominated by simple shear near the dyke walls is believed to produce particle shape preferred orientations (SPO) with angles up to 30° with the flow plane (Blanchard *et al.* 1979; Blumenfeld & Bouchez 1988; Benn & Allard 1989; Correa-Gomes *et al.* 2001). A magnetic foliation representative of that petrofabric has been called 'normal' magnetic fabric (e.g. see reviews of Rochette *et al*. 1992 and 1999) and then assumed as representative of magma flow direction. When high angular differences are observed with the dyke wall, fabrics have been called 'abnormal'. These 'abnormal' magnetic fabrics have been interpreted as a result of late (post-emplacement) disturbances caused by the superposition of secondary fabrics due to different reasons (acting concurrently or independently): mechanical (tectonics), chemical (hydrothermal and/or metamorphic) and/or magnetic, such as the presence of SD particles (e.g. Park *et al.* 1988; Potter & Stephenson 1988; Staudigel *et al*. 1992; Raposo & Ernesto 1995; Varga *et al*. 1998; Herrero-Bervera *et al*. 2002; Borradaile & Gauthier 2003; Raposo *et al*. 2004).

Dragoni *et al*. (1997) and Cañón-Tapia & Chávez-Álvares (2004) developed a theoretical model based on Jeffery's (1922) equations, showing that the principal directions of the magnetic susceptibility ellipsoid are not exclusively associated with the flow direction or with the dyke plane, but also with mineral shape, elliptical movement of the particles and strain partitioning within dyke. These authors were able to reproduce different magnetic fabrics, previously interpreted as 'abnormal', therefore not necessarily related to features developed during post-emplacement processes. On the other hand, according to Féménias *et al.* (2004), the strain regime of a Newtonian fluid can evolve along dyke cross-sections from simple shear near the margins to mainly pure shear towards the core. A magma flow under pure shear is able to re-orient the larger surfaces of the minerals during magma compaction to a plane approximately perpendicular to the flow direction, therefore generating an 'abnormal' magnetic fabric. Dawson & Hargraves (1985) found by computer modelling two possible configurations for such abnormal fabric regarding principal axes orientation relative to dyke trend: (1) if K_1 is aligned with the dyke trend and K_3 perpendicular to the dyke walls, magma is in motion and (2) if K_1 is perpendicular to dyke walls, magma is stationary. Such kind of fabric with K_1 aligned with the dyke trend was obtained by Park *et al.* (1988) and Raposo & Ernesto (1995) and interpreted as a response to the freezing of the upper part of the dyke, so, stopping the vertical propagation of magma and promoting stress relaxation by subhorizontal propagation of the fracture along which the dyke is intruding. From analogue modelling, Kratinová *et al.* (2006) were able to reproduce similar magnetic fabrics as a response to the evolution of different strain regimes.

However, the first criterion to use AMS to infer magma flow is that composite fabric involving inverse fabric be eliminated; therefore, mostly type 3 is used. However, two sites of type 3 (DE-NW1 and DE-FL) show strongly 'abnormal' fabric (Rochette *et al.* 1999) and were also discarded. The strong 'abnormal' fabric in these two sites

(K_3 mostly aligned with the dyke trend) corresponds to magnetic foliations at a very high angle to the dyke wall. One explanation to this is that the fabric was acquired by dominant pure shear during static magma compaction, as a response to mechanisms that hamper the vertical propagation of magma (e.g. freezing of the upper part of the dyke or fracture strangulations), thus promoting stress release by subhorizontal propagation of the fracture for magma injection (Park *et al.* 1988; Raposo & Ernesto 1995). At station VF, we have, in addition, indication of downward flow close to the margin ('normal' fabric) and a more complex flow in the core, shown by an 'abnormal' fabric. Field observation shows that ~2 m above the sampled cross-section, the dyke shows an asymmetrical strangulation, with dyke thickness reducing from 6 m at the bottom to approximately 1 m at the top, due to the gradual closure of the NW wall. Therefore, with hampered vertical propagation, one can expect that magma flow becomes more complex, which is reflected in the measured fabrics. For some fabrics of type 2, inverse fabric has possibly a weak effect in the composite fabric. In addition, part of these type 2 fabrics are not 'abnormal', and we used, as a limit, an α value (30°) for the 'abnormal' sites (e.g. Blanchard *et al.* 1979; Blumenfeld & Bouchez 1988; Benn & Allard 1989; Rochette *et al*., 1999; Correa-Gomes *et al.* 2001). Among the 12 sites finally chosen for flow determination, 9 are very close to the dyke wall. This indicates that flow approximates simple shear close to dyke walls, where differential flow is expected to take place due to friction and viscous drag. As shown in Table 1, the fabric is mostly 'abnormal', away from the walls (especially in thick dykes). This can be interpreted in two ways: (1) the reference is not anymore the dyke wall and/or (2) the flow in core domains of thick dykes greatly departs from simple shear.

Regarding opposite walls of the dyke, the imbrication angle is expected to be in opposite directions, giving a symmetrical disposition of the magnetic foliation relative to the mid plane of the dyke. The intersection of the magnetic foliation of the two sides of the dyke (i.e. the magnetic zone axis; Henry 1997), is a line perpendicular to the flow direction. In the plane perpendicular to this line, flow direction corresponds to the intersection with the plane of the dyke. Flow sense is toward the acute angle of imbrication. The interpretation of imbrication in all the 12 sites, mostly, rather suggests vertical movement of the magma in 7 sites, 3 of which seem to be more compatible with a downward movement of magma (AL-SE1, DE-C1 and VF-SE1) and 4 sites in which an upward magma flow is suggested by the observed imbrications (DE-SE, JU1-B, PO2-SE and PO4-SE). In three other sites flow is dominantly horizontal, AL-SE2 and MB1-NW, with flow probably toward SW, and PO5-NW, probably toward NE. The two remaining sites, MB2-NW1 and EL1-C, show oblique flow probably toward NE and SW, respectively. Only 4 of the 12 retained sites show K_1 related with the flow direction determined by imbrication analysis: K_1 in sites DE-C1 and DE-SE and K_2 in sites JU1-B and AL-SE2, in agreement with previous works (e.g. Baer 1995; Moreira *et al*. 1999; Geoffroy *et al.* 2002; Callot & Guichet 2003), Thus, K_1 is not always a suitable indicator of magma flow direction.

To envisage the magma flow for the whole dyke scale, K_1 and K_3 of all the retained sites were rotated to a common frame, which provides the dyke plane as vertical and N–S (Fig. 12), an approach already adopted by Rochette *et al*. (1999). Most data show that the magnetic foliation has the same direction as the dyke plane, with an inclination ranging between 45° and 90°. Such variations in dip and the subhorizontal orientation of the magnetic zone axis (aligned with the dyke azimuth), indicate a vertical-dominated magma flow.

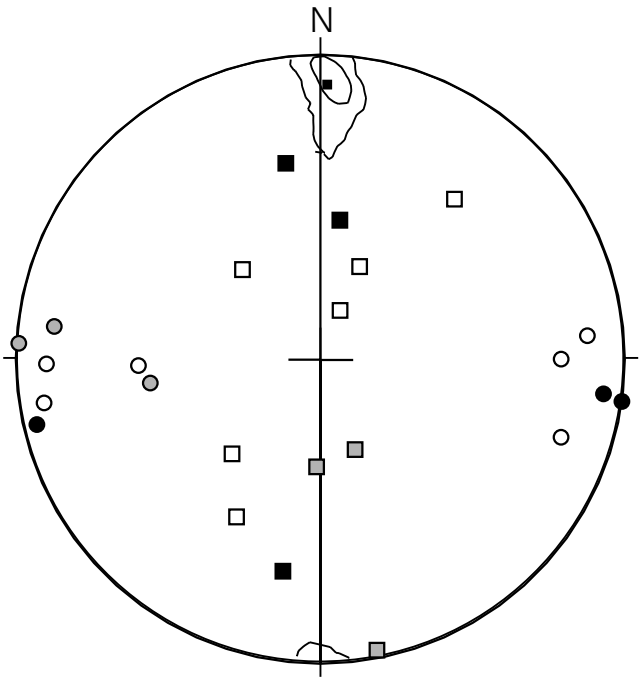

Figure 12. Stereographic projection (lower hemisphere) for sites retained for magma flow determination after rotation to the same frame according to the attitude of each segment of the dyke. White, grey and black symbols correspond to data from SE margins, corer domains and NW margins, respectively. Zone axis confidence ellipse with confidence zones at 95 and 63 per cent of the 10 000 bootstrap re-sampling.

9 CONCLUSIONS

The present study shows that the effects of metasomatism on rock mineralogy are important; however, they vary according to location within the dyke and to the fluid/rock ratios during the early stages of dyke cooling. The metasomatic processes, which took place at relatively lower temperatures, can greatly influence anisotropy degree and mean susceptibility, as shown for site DE-FL, the only one strongly affected by metasomatism.

Petrography, SEM and bulk magnetic analyses show a high-temperature oxidation-exsolution event experienced by the very early Ti-spinels during the early stages of magma cooling. Exsolution was observed in central domains of the thick dyke segments, which can favour a slow cooling rate. Exsolution reduced the grain size of the magnetic carrier (MD to SD transformation), thus producing inverse fabrics. These are likely responsible for a significant number of the 'abnormal' fabrics, which make the interpretation of magma flow much more complex. However, other mechanisms also likely disturbed the magnetic fabric in part of the sites, mostly in core domains.

By rejecting composite fabrics involving inverse fabric for magma flow determination, we have reduced the number of relevant sites to 12. At these sites, the imbrication angle of the magnetic foliation strongly suggests variable flow, with end-members indicating vertical-dominated flow (seven sites) or horizontal-dominated flow (three sites). Flow direction can be to the SW or to the NE and downward or upward. This is not surprising in the flow of a magma trying to find its way to the surface through an irregular fracture, forced to open (horizontally and vertically) along a heterogeneous crust, and experiencing the effects of magma cooling and contraction and pressure and temperature gradients.

ACKNOWLEDGMENTS

Funding by TEAMINT (POCTI/CTE/48137/2002), CNRS, France; GRICES, Portugal; Acção Integrada CRUP–CSIC (n° E21–03) and Gulbenkian Foundation is acknowledged. We thank C. Aubourg and E. Cañón-Tapia for constructive and detailed reviews and editorial work by E. Appel, which helped to improve the quality of this manuscript. We thank M. Le Goff for technical assistance during experimental work. We also thank Thierry Aigouy and Philippe de Perseval for Technical assistance in SEM analyses and Jean-Luc Bouchez for discussions.

REFERENCES

Ade-Hall, J.M., Khan, M.A. Dagley, P. & Wilson, R.I., 1968. A detailed opaque petrological and magnetic investigation of a single tertiary lava flow from Skye, Scotland, I: iron–titanium oxide petrology, *Geophys. J. R. astr. Soc.,* **16,** 375–388.

Ade-Hall, J.M., Palmer, H.C. & Hubbard, T.P., 1971. The magnetic and opaque petrological response of basals to regional hydrothermal alteration, *Geophys. J. R. astr. Soc.,* **24,** 137–174.

Archanjo, C.J., Araújo, M.G.S. & Launeau, P., 2002. Fabric of the Rio Ceará-Mirin mafic dike swarm (northeastern Brazil) determined by anisotropy of magnetic susceptibility and image analysis, *J. geophys. Res.,* **107,** B3, 10.1029

Baer, G., 1995. Fracture propagation and magma flow in segmented dykes: field evidences and fabric analyses, Makhtesh Ramon, Israel, in *Physics and Chemistry of Dykes*, pp. 125–140, eds Baer, G., Heimann, A., Balkerna, Rotterdam.

BENN, K. & Allard, B., 1989. Preferred mineral orientations related to magmatic flow in ophiolite layered gabbros, *J. Petrol.,* **30,** 925–946.

Blanchard, J.P., Boyer, P. & Gagny, C., 1979. Un nouveau critère de sens de mise en place dans une caisse filionienne: le "pincement" des minéraux aux éponte, *Tectonophysics,* **53,** 1–25.

Blumenfeld, P. & Bouchez, J.-L., 1988. Shear criteria in granite and migmatite deformed in the magmatic and solid states, *J. Struct. Geol.,* **10,** 361–372.

Borradaile, G.J. & Gauthier, D., 2003. Interpreting anomalous magnetic fabrics in ophiolite dikes, *J. Struct. Geol.,* **25,** 171–182.

Borradaile, G.J. & Gauthier, D., 2006. Magnetic studies of magma-supply and sea-floor metamorphism: Troodos ophiolite dikes, *Tectonophysics,* **v. 418,** 75–92.

Borradaile, G.J. & Henry, B., 1997. Tectonic applications of magnetic susceptibility and its anisotropy, *Earth-Sci. Rev.,* **42,** 49–93

Butler, R., 1992. *Paleomagnetism: Magnetic Domains to Geologic Terranes*, *Blackwell Science Inc.,* 250 pp.

Callot, J.P., Geoffroy, L., Auborg, C., Pozzi, J.P. & Mege, D., 2001. Magma flow directions of shallow dykes from the East Greenland volcanic margin inferred from magnetic fabric studies, *Tectonophysics,* **335,** 313–329.

Callot, J.P. & Guichet, X., 2003. Rock texture and magnetic lineation in dykes: a simple analytical model, *Tectonophysics,* **366,** 207–222.

Cañón-Tapia, E., 2004. Anisotropy of magnetic susceptibility of lava flows and dykes: a historical account. in *Magnetic Fabric Methods and Applications*, Vol.238, pp. 205–225, eds Martin Hernandez, F., Aubourg, C., Jackson, M. & Luneburg, C. , Geol. Soc. Lond., Spec. Publ.

Cañón-Tapia, E. & Chávez-Álvarez, M.J., 2004. Theoretical aspects of particle movement in flowing magma: implication for the anisotropy of magnetic susceptibility of dykes and lava flows, in *Magnetic Fabric Methods and Applications*, Vol. **238**, eds Martin Hernandez, F., Aubourg, C., Jackson, M. & Luneburg, C., Geol. Soc. Lond., Spec. Publ..

Cébriá, J.M., López-Ruiz, J., Doblas, M., Martins, L.T. & Munha, J., 2003. Geochemistry of the Early Jurassic Messejana-Plasencia dyke (Portugal – Spain); Implications on the origin of the Central Atlantic Magmatic Province, *J. Petrol.,* **44**(33), 547–568.

Correa-Gomes, L.C., Souza Filho, C.R., Martins, C.J.F.N. & Oliveira, E.P., 2001. Development of symmetrical and asymmetrical fabrics in sheet-like igneous bodies: the role of magma flow and wall-rock displacements in theoretical and natural cases, *J. Struct. Geol.,* **23,** 1415–1428.

Dawson, E. M. & Hargraves R. B., 1985. Anisotropy of magnetic susceptibility as an indicator of magma flow directions in diabase dykes (abstract), *Eos, Trans. Am. geophys. Un.,* **66,** 251.

Day, R., Fuller, M. & Schmidt, V.A., 1977. Hysteresis properties of titanomagnetites: grain size and compositional dependence, *Phys. Earth planet. Inter.,* **13,** 260–267.

de Bruijne C.H., 2001. Denudation, intraplate tectonics and far field effects. An integrated apatite fission track study in central Spain (Published), *PhD thesis*. Vvrije Universiteit Amsterdam, the Nederlands.

Del Valle Lersundi, J., 1959. Sobre la posible existencia de una importante falla en el SO de la Península, *Not. Com. Inst. Geol. Minero España,* **56,** 103–108.

Dragoni, M., Lanza, R. & Tallarico, A., 1997. Magnetic anisotropy produced by magma flow: theoretical model and experimental data from Ferrar dolerite sill (Antarctica), *Geophys. J. Int.,* **128,** 230–240.

Dunlop, D.J., 2002. Theory and application of the Day plot (Mrs/Ms versus Hcr/Hc), 1: theoretical curves and tests using titanomagnetite data, *J. geophys. Res.,* **107**(B3), doi:10.1029/2001, 2002.

Dunlop, D.J. & Özdemir, Ö., 1997. *Rock Magnetism: Fundamentals and Frontiers*, Cambridge University Press, Cambridge, UK, 573 pp.

Dunn, A.M., Reynolds, P.H., Clarke, D.B. & Ugidos, J.M., 1998. A comparison of the age and composition of the Shelburne dyke, Nova Scotia, and the Messejana dyke, Spain, *Can. J. Earth Sci.,* **35,** 1110–1115.

Ernst, R.E. & Baragar, W.R.A., 1992. Evidence from magnetic fabric for the flow pattern of magma in the Mackenzie giant radiating dyke swarm, *Nature,* **356,** 511–513.

Ernst, R.E., Head, J.W., Parfitt, E., Grosfils, E. & Wilson, L., 1995. Giant radiating dyke swarms on Earth and Venus, *Earth-Sci. Rev.* **39,** 1–58.

Feinberg, J.M., Harrison, R.J., Kasama, T., Dunin-Borkowski, R.E., Scott, G.R. & Renne, P.R., 2006. Effects of internal mineral structures on the magnetic remanence of silicate-hosted titanomagnetite inclusions: an electron holography study, *J. geophys. Res.,* **111,** B12S15, doi:10.1029/2006JB004498.

Ferré, E.C., 2002. Theoretical models of intermediate and inverse AMS fabrics, *Geophys. Res. Lett.,* **29,** doi:10.1029/2001GL014367.

Féménias, O., Diot, H., Berzad, T., Gauffriau, A. & Demaiffe, D., 2004. Asymmetrical to symmetrical magnetic fabric of dikes: paleo-flow orientations and Paleo-stresses recorded on feeder-bodies from the Motru Dike Swarm (Romania), *J. Struct. Geol.,* **26,** 1401–1418.

Geoffroy, L., Callot, J.P., Aubourg, C. & Moreira, M., 2002. Magnetic and plagioclase linear fabric discrepancy in dykes: a new way to define the flow vector using magnetic foliation, *Terra Nova,* **14,** 183–190.

Hargraves, R.B., Johnson, D. & Chan, C.Y., 1991. Distribution anisotropy: the cause of AMS in igneous rocks? *Geophys. Res. Lett.,* **18,** 2193–2196.

Henry, B., 1974. Sur l'anisotropie de susceptibilité magnétique du granite récent de Novate (Italie du Nord), *C. R. Acad. Sci. Paris,* **278C,** 1171–1174.

Henry, B., 1997. The magnetic zone axis: a new element of magnetic fabric for the interpretation of the magnetic lineation, *Tectonophysics,* **271,** 325–329.

Herrero-Bervera E., Canon-Tapia E., Walker G.P.L. & Guerrero-Garcia J.C., 2002 The Nuuanu and Wailua giant landslides: insights from paleomagnetic and anisotropy of magnetic susceptibility (AMS) studies, *Phys. Earth planet. Inter.,* **129**(1–2), 83–98.

Hext, G., 1963. The estimation of second-order tensor, with related tests and designs, *Biometrika,* **50,** 353–357.

Hrouda, F., Chlupacova, M. & Novak, J.K., 2002. Variations in magnetic anisotropy and opaque mineralogy along a kilometer deep profile within a vertical dyke of the syenogranite porphyry at Cínovec (Czech Republic), *J. Volc. Geoth. Res.,* **113,** 37–47.

Hunt, P., Moskowitz, B.M. & Banerjee, S.K., 1995. *Rock Physics & Phase Relations: A Handbook of Physical Constants*, AGU, Washington, DC, USA, 236 p.

Jeffery, G.B., 1922. The motion of ellipsoidal particles immersed in a viscous fluid. *Proc. R. Soc. Lond., A,* **102,** 161–179.

Jelinek, V., 1978. Statistical processing of magnetic susceptibility measured in groups of specimens, *Stud. Geophys. Geod.,* **22,** 50–62.

Jelinek, V., 1981. Characterization of the magnetic fabric of rocks, *Tectonophysics,* **79,** 63–67.

Jelinek, V., 1996. Theory and measurement of the anisotropy of isothermal remanent magnetization of rocks, *Travaux Geophys*. **37,** 124–134.

Khan, M.A., 1962. The anisotropy of magnetic susceptibility of some igneous and metamorphic rocks, *J. geophys. Res.,* **67**(7), 2874–2885.

Knight, M.D. & Walker, G.P.L., 1988. Magma flow directions in dikes of the Koolau Complex, Oahu, determined from magnetic fabric studies, *J. geophys. Res.,* **93,** B5, 4301–4319.

Krasa, D. & Herrero-Bervera, E., 2005. Alteration induced changes of magnetic fabric as exemplified by dykes of the Koolau volcanic range, *Earth planet. Sci. Lett.,* **240,** 445–453.

Kratinová, Z., Závada, P., Hrouda, F. & Schulmann, K., 2006. Non-scaled analogue modelling of AMS development during viscous flow: a simulation on diapir-like structures, *Tectonophysics* **418,** 51–61

Kruiver, P.P., Dekkers, M.J. & Heslop, D., 2001. Quantification of magnetic coercivity components by the analysis of acquisition curves of isothermal remanent magnetization, Earth planet, *Sci. Lett.,* **189,** 269–276.

Lattard, D., Engelmann R., Kontny A. & Sauerzapf U., 2006. Curie temperatures of synthetic titanomagnetites in the Fe-Ti-O system: effects of composition, crystal chemistry, and thermomagnetic methods, *J. geophys. Res.,* **111,** B12S28.

Lefort, J.P., Aifa, T. & Hervé, F., 2006. AMS criteria for determining the azimuth and dip of a subduction zone from a mafic dyke swarm. in: *In Dyke Swarms – Time Markers of Crustal Evolution*, pp. 49–62, eds Hanski, E., Mertanen, S., Rämö, T. & Vuollo, J., Taylor & Francis Group, London,UK.

Lister, J.R. & Kerr, R.C., 1991. Fluid-mechanical models of crack propagation and their application to magma transport in dykes, *J. geophys. Res.,* **96,** 10 049–10 077.

Lowrie, W., 1990. Identification of ferromagnetic minerals in a rock by coercivity and unblocking temperature properties, *Geophys. Res. Lett.,* **17,** 159–162.

Marques, F.O., Mateus, A. & Tassinari, C., 2002. The late-Variscan fault network in central-northern Portugal (NW Iberia): a re-evaluation, *Tectonophysics,* **359,** 255–270

Martins, L.T., 1991. Actividade Ígnea Mesozóica em Portugal (contribuição petrológica e geoquímica), *Ph.D. thesis*. Universidade de Lisboa, 418 pp.

Marzoli, A., Renne, P.R., Piccirillo, E.M., Ernesto, M., Belliene, G. & De Min, A., 1999. Extensive 200-million-year-old continental flodd basalts of the Central Atlantic Magmatic Province, *Science,* **284,** 616–618.

May, P.R., 1971. Pattern of Triassic-Jurassic diabase dikes around the North Atlantic in the context of predrift position of the continents, *Geol. Soc.. Am. Bull.,* **82,** 1285–1292.

Moreira, M., Geoffroy, L. & Pozzi, J.-P., 1999. Ecoulement magmatic dans les dykes du point chaud des Açores: etude préliminaire par anisotropie de susceptibilité magnétique ASM dans l'Île de San Jorge, *C. R. Acad. Sci. Paris,* **329,** 15–22.

O'Reilly, W., 1984. *Rock and Mineral Magnetism*. Blackie, Glasgow and London, & Chapman and Hall, New York, 220 pp.

Park, J.K., Tanczyk, E.I., & Desbarats, A., 1988. Magnetic Fabric and Its Significance in the 1400 Ma Mealy Diabase Dykes of Labrador, Canada, *J. geophys. Res.,* **93,** 13 689–13 704.

Palencia-Ortas, A., Osete, M.L., Vegas, R. & Silva, P.F., 2006. Paleomagnetic study of the Messejana-Plasencia dyke (Portugal and Spain): a lower Jurassic paleopole for the Iberian plate. *Tectonophysics,* **420,** 455–472

Perrin, M., Prévot, M. & Mankinen, E., 1991. Low intensity of the geomagnetic field in Early Jurtassic time, *J. geophys. Res.,* **93,** 14 197–14 210.

Petrovský, E. & Kapička A, 2006. On determination of the Curie point from thermomagnetic curves, *J. geophys. Res.,* **111,** B12S27, doi:10.1029/2006JB004507

Platen, I.M. & Watterson, J., 1987. Magma flow and cristtalization in dike fissures, in, *Mafic Dyke Swarms*, Vol. **34,** pp. 65–73, eds Halls, H.C. & Fahrig, W.F., Geol. As. Can. Spec. Pap.

Potter, D.K. & Stephenson, A., 1988. Single-domain particles in rocks and magnetic fabric analysis, *Geophys. Res. Lett.,* **15,** 1097–1100.

Rapaille, C., Marzoli, A., Bertrand, H., Féraud, G., Reisberg, L. & Fontignié, D., 2003. Geochemistry and $^{40}Ar/^{39}Ar$ age of the European part of the Central Atlantic Magmatic Province, in *Proceedings of the EUG-AGU-EGS Joint Assembly* 6–11 April 2003, Nice.

Raposo, M. & Ernesto, M., 1995. Anisotropy of magnetic susceptibility in the Ponta-Grossa dyke swarm (Brazil) and its relationship with magma flow direction, *Phys. Earth planet. Inter*., **87** (3–4), 183–196.

Raposo, M.I.B, Chaves, A.O., Lojkasek-Lima, P., D'Agrella-Filho, M.S. & Teixeira, W., 2004. Magnetic fabrics and rock magnetism of Proterozoic dike swarm from the southern São Francisco Craton, Minas Gerais State, Brazil, *Tectonophysics,* **378,** 43–63

Robertson, D.J. & France, D.E., 1994. Discrimination of remanence-carrying minerals in mixtures, using isothermal remanent magnetisation acquisition curves, *Phys. Earth planet. Inter.,* **82,** 223–234.

Rochette, P., 1988. Inverse magnetic fabric carbonate bearing rocks, Earth Planet, *Sci. Lett.,* **90,** 229–237.

Rochette, P., Jackson, M. & Aubourg, C., 1992. Rock magnetism and the interpretation of anisotropy of magnetic susceptibility, *Rev. Geophys.,* **30,** 209–226.

Rochette, P., Aubourg, C. & Perrin, M., 1999. Is this magnetic fabric normal? A review and case studies in volcanic formations, *Tectonophysics,* **307,** 219–234.

Rubin, A.M., 1995. Propagation of magma-field cracks, *An. Rev. Earth planet. Sci.,* **23,** 287–336.

Schermerhorn, L.J.G., Priem, H.N.A., Boelrijk, N.A.I.M., Hebeda, E.H., Verdurmen, R.H. & Verschure, E.A.Th., 1978. Age and origin of the Messejana Dolerite fault-dike system (Portugal and Spain) in the light of the opening of the North Atlantic Ocean, *J. Geol.,* **86,** 299–309.

Schott, J.J., Montigny, R. & Thuizat, R., 1981. Paleomagnetism and potassium-argon age of the Messejana Dike (Portugal and Spain): angular limitation to the rotation of the Iberian Peninsula since the Middle Jurassic, *Earth planet. Sci. Lett.,* **53,** 457–470.

Silva, P.F., Marques, F.O., Henry, B., Mateus, A., Lourenco, N. & Miranda, J.M., 2004. Preliminary results of a study of magnetic properties in the Foum-Zguid dyke (Morocco), *Phys. Chem. Earth,* **29,** 909–920.

Staudigel, H., Gee, J., Tauxe, L. & Varga, R.J., 1992. Shallow intrusive directions of sheeted dikes in the Troodos ophiolite: anisotropy of magnetic susceptibility and structural data, *Geology,* **20,** 841–844.

Stephenson, A., Sadikum S. & Potter D. K., 1986 A theoretical and experimental comparison of the anisotropies of magnetic susceptibility and remanence in rocks and minerals, *Geophys. J. R. astr. Soc.,* **84,** 185–200.

Tarling, D.H. & Hrouda, F., 1993. *The Magnetic Anisotropy of Rocks*, pp. 1–217, Chapman & Hall, London, UK.

Tauxe, L., Gee, J.S. & Staudigel, H., 1998. Flow directions in dikes from anisotropy of magnetic susceptibility data: the bootstrap way, *J. geophys. Res.,* **103**(B8), 17 775–17 790.

Topplis, M.J. & Carroll, M.R., 1995. An experimental study of the influence of oxygen fugacity on Fe-Ti oxide stability, phase relations, and mineral-melt equilibria in ferro-basaltic systems, *J. Petrol.,* **36,** 1137–1170.

Torre de Assunção, C., 1949. Sobre uma intrusão dolerítica no Antracolítico do Baixo-Alentejo, *Bol. Soc. Portuguesa Ciênc. Naturais,* **2,** 66–74.

Varga, R.J., Gee, J.S., Staudigel, H. & Tauxe, L., 1998. Dike surface lineations as magma flow indicators within the sheeted dike complex of the Troodos ophiolite, Cyprus, *J. geophys. Res.,* **103**(B3), 5241–5256.

Vegas, R., 2000. The intrusion of the Plasencia (Messejana) dyke as part of the Circum-Atlantic Early Jurassic magmatism: tectonic implications in the southwester Iberian Peninsula, *Geogaceta,* 175–178.

Wang, D., Van Der Voo, R. & Peacor, D.R., 2006. Low-temperature alteration and magnetic changes of variably altered pillow basalts Geophys, *J. Int.,* **164,** 25–35.

Waychunas, G.A., 1991. Crystal chemistry of oxides and oxyhydroxides in oxide minerals: petrologic and magnetic significance (ed. Lindsley, D.H.). *Rev. Mineral*. **25,** 11–68.

Wilson, R.I., Haggerty, S.E. & Watkins, N.D., 1968. Variation of paleomagnetic stability and other parameters in a vertical traverse of a single Icelandic lava, *Geophys. J. R. astr. Soc.,* **16,** 79–96.

Zbyszewski, G. & Freire de Andrade, R., 1957. Nota preliminary sobre a geologia da região de Aljustrel. Assoc. Portuguesa Progresso Ciênc., 23 Congr, *Luso- Espanhol.,* **5,** 5–13.